

## Two Configurations of the Western Arctic Shelfbreak Current in Summer

WILKEN-JON VON APPEN

*Massachusetts Institute of Technology–Woods Hole Oceanographic Institution Joint Program in Oceanography,  
Woods Hole, Massachusetts*

ROBERT S. PICKART

*Department of Physical Oceanography, Woods Hole Oceanographic Institution, Woods Hole, Massachusetts*

(Manuscript received 3 February 2011, in final form 29 June 2011)

### ABSTRACT

Data from a closely spaced array of moorings situated across the Beaufort Sea shelfbreak at 152°W are used to study the Western Arctic Shelfbreak Current, with emphasis on its configuration during the summer season. Two dynamically distinct states of the current are revealed in the absence of wind, with each lasting approximately one month. The first is a surface-intensified shelfbreak jet transporting warm and buoyant Alaskan Coastal Water in late summer. This is the eastward continuation of the Alaskan Coastal Current. It is both baroclinically and barotropically unstable and hence capable of forming the surface-intensified warm-core eddies observed in the southern Beaufort Sea. The second configuration, present during early summer, is a bottom-intensified shelfbreak current advecting weakly stratified Chukchi Summer Water. It is baroclinically unstable and likely forms the middepth warm-core eddies present in the interior basin. The mesoscale instabilities extract energy from the mean flow such that the surface-intensified jet should spin down over an *e*-folding distance of 300 km beyond the array site, whereas the bottom-intensified configuration should decay within 150 km. This implies that Pacific Summer Water does not extend far into the Canadian Beaufort Sea as a well-defined shelfbreak current. In contrast, the Pacific Winter Water configuration of the shelfbreak jet is estimated to decay over a much greater distance of approximately 1400 km, implying that it should reach the first entrance to the Canadian Arctic Archipelago.

### 1. Introduction

The Western Arctic Shelfbreak Current advects Pacific-origin waters eastward along the edge of the narrow ( $\approx 50$  km) and shallow ( $< 50$  m) Beaufort Sea shelf. Although the current influences local conditions on the Beaufort shelf such as ice cover and nutrient supply available for biological production, it also influences the interior Canada Basin. For example, the lateral transport of properties away from the current, via processes such as baroclinic instability (e.g., Spall et al. 2008), helps ventilate the cold halocline of the interior Canada Basin (Pickart et al. 2005). Such mesoscale variability of the current also impacts the pathways of Pacific Water (PW) through the Arctic Ocean and ultimately into the North Atlantic.

Pacific Water first enters the Arctic Ocean through Bering Strait, where, in the multiyear mean, 0.8 Sv ( $1 \text{ Sv} \equiv 10^6 \text{ m}^3 \text{ s}^{-1}$ ) of water flows from the Bering Sea to the Chukchi Sea, though this number varies seasonally from 0.4 to 1.3 Sv (Woodgate et al. 2005b). Both of these shelf seas are shallow ( $< 50$  m) and are strongly influenced by wind forcing and the seasonal sea ice melt/thaw cycle. The northward flow of Pacific Water is driven by a pressure head that arises because the Pacific is significantly fresher than the Atlantic (Woodgate and Aagaard 2005; Huang and Schmitt 1993). This flow persists despite the fact that the predominant winds in the Bering Strait are northerly and therefore oppose the current (Overland and Roach 1987). Three types of Pacific Water have been identified in the strait based on their distinct sources (Woodgate and Aagaard 2005): nutrient-rich Anadyr Water flows through the western (Russian) passage of Bering Strait, whereas the generally saltier and colder Bering shelf waters occupy the eastern (United States) passage. The third water mass is Alaskan Coastal Water (ACW) which is

---

*Corresponding author address:* Wilken-Jon von Appen, MS 21, Woods Hole Oceanographic Institution, Woods Hole, MA 02543.  
E-mail: wilken@mit.edu

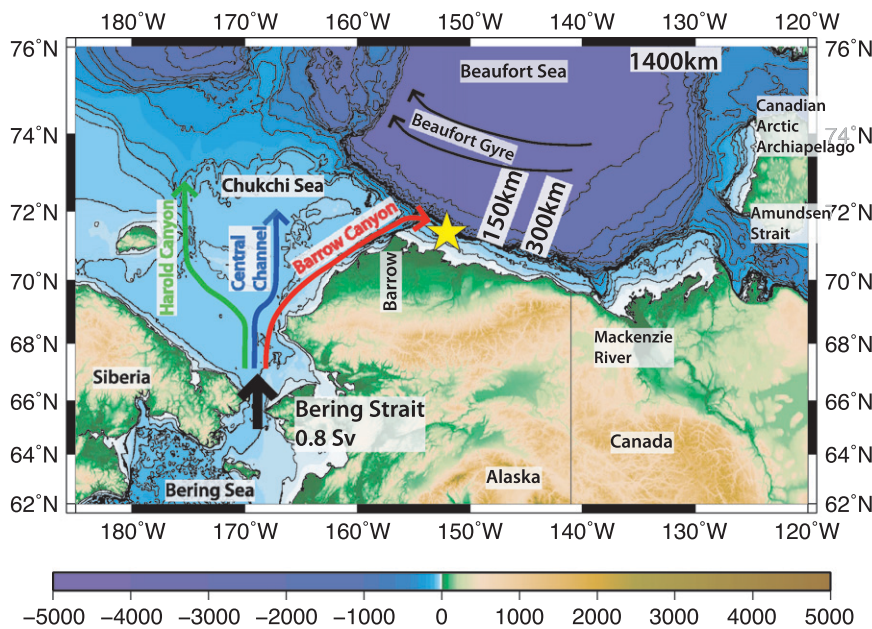


FIG. 1. Map of the study region in the western Arctic, including geographical names. Elevation is shown in color (data from Jakobsson et al. 2008). The circulation is represented schematically by arrows (see text). The mooring array at 152°W is indicated by the yellow star, and downstream distances of 150, 300, and 1400 km from the array are marked.

transported seasonally by the Alaskan Coastal Current (ACC) in the easternmost part of the strait. This current originates from river runoff into the Gulf of Alaska and Bering Sea (Weingartner et al. 2005). Although there is general agreement in the literature on the nomenclature of the Alaskan Coastal Current and the fresh, warm water it advects, the remaining water masses, which change seasonally, are less precisely defined. Furthermore, significant water mass transformation takes place north of the strait in the Chukchi Sea (e.g., Weingartner et al. 1998).

The topography of the Chukchi Sea helps channel the Pacific Water into three distinct northward-flowing branches, as shown in Fig. 1 (Paquette and Bourke 1981; for a more recent treatment, see Woodgate et al. 2005a). The eastern branch generally follows the Alaskan coast into Barrow Canyon; in summertime, this is the pathway of the Alaskan Coastal Current. The middle branch extends through the depression between Hanna and Herald shoals, known as the Central Channel (Weingartner et al. 1998), and the western branch flows through Herald Canyon east of Wrangel Island (Pickart et al. 2010). Both summer and winter water masses are advected in each of these branches. However, uncertainties remain regarding the relative timing of the seasonal transition and the potential interaction of the summer and winter waters within the individual branches. Synoptically, as well as seasonally, the partitioning of transport varies between the three branches as

shown by numerical models (e.g., Winsor and Chapman 2004; Panteleev et al. 2010).

Pacific Water is found throughout the Arctic Ocean and has important impacts there. The halocline is in part maintained by an influx of freshwater from Bering Strait, which together with precipitation and river runoff balances the upward mixing of salt from the Atlantic Water (AW) layer (Aagaard et al. 1981). As warm Pacific Water enters the Arctic in the beginning of summer, it is able to facilitate ice melt. For the extreme ice minimum year of 2007, Woodgate et al. (2010) argued that the heat flux through Bering Strait was sufficient to account for a third of the sea ice retreat. Pacific Water also carries nutrients required for primary productivity into the Arctic Ocean. As a result of upwelling in the Bering Sea shelf, the Anadyr Water is particularly high in nutrient concentration (Sambrotto et al. 1984), whereas the Alaskan Coastal Water is nutrient poor because it is composed of river runoff mixed with ambient oceanic water (Weingartner et al. 2005).

Within the halocline layer of the interior western Arctic Ocean, there are both a local temperature minimum near 150–200 m, attributed to Pacific Winter Water (PWW), and an overlying temperature maximum attributed to Pacific Summer Water (PSW; Steele et al. 2004). The winter water is formed during freeze up in the Bering and Chukchi Seas (Muench et al. 1988; Weingartner et al. 1998). Throughout the winter season, it further densifies because of brine rejection during

freezing within leads and polynyas in the Chukchi Sea (Cavaliere and Martin 1994). The densest variety of winter water is referred to as hypersaline water (Weingartner et al. 1998). Pacific Summer Water comes in two varieties that have a multitude of naming conventions found in the literature. The first, characterized by temperatures near  $-1^{\circ}\text{C}$  and salinities greater than 32, has been referred to as Summer Bering Sea Water by Steele et al. (2004) and Western Chukchi Summer Water by Shimada et al. (2001). In the present study, we simply call it Chukchi Summer Water (CSW). The second is the Alaskan Coastal Water, with salinities between 31 and 32. In some other places, this has also been called Eastern Chukchi Summer Water after it spreads into the interior basin (e.g., Shimada et al. 2001). Here, we adopt the former terminology.

Although climatologies (e.g., Environmental Working Group 1998) indicate that the cold and warm temperature extrema within the halocline layer exist over a broad region of the Canada basin, local measurements from drifting platforms often reveal small-scale features with anomalously cold and warm signatures relative to the ambient water (e.g., Manley and Hunkins 1985; Muench et al. 2000; A. Plueddemann and R. Krishfield 2007, personal communication; Timmermans et al. 2008). It is now known that such features are usually associated with subsurface eddies of Pacific Water. The majority of the eddies are middepth-intensified cold-core anticyclones with diameters of 10–20 km. A. Plueddemann and R. Krishfield (2007, personal communication) found that, on average, an eddy was encountered every 100 km of drift of their instrument platform. Azimuthal velocities of up to  $0.4\text{ m s}^{-1}$  at depths between 50 and 200 m were observed in the eddies compared to the mean flow of  $<0.05\text{ m s}^{-1}$  at these depths. In general, the centers of the cold-core eddies have temperature anomalies  $\geq 0.1^{\circ}\text{C}$  and are not warmer than  $-1^{\circ}\text{C}$ . In addition to these cold features, shipboard measurements north of the Chukchi Sea have revealed a shallower ( $<100\text{ m}$ ) warm-core subsurface eddy ( $\approx 0^{\circ}\text{C}$ ), as well as a surface-intensified warm-core ( $>2^{\circ}\text{C}$ ) anticyclone containing Alaskan Coastal Water (Pickart and Stossmeister 2008). Thus, eddies of the three different seasonal Pacific Water masses noted above (winter water, summer water, and Alaskan Coastal Water) have been observed.

There have been a number of explanations for the formation of the eddies. A series of studies suggested that the cold-core eddies can originate in the interior basin because of brine rejection during the opening of leads (Chao and Shaw 1996, 1998, 1999). Synoptic winds over the interior Arctic Ocean have also been suggested as an eddy generation mechanism (see the discussion in Hunkins 1974). However, Hunkins (1974) argued that

such processes in the interior Arctic occur on scales inconsistent with the dimensions of the eddies. In particular, the wind forcing occurs on scales that are too large, whereas the brine rejection occurs on scales that are too small. This led Hunkins (1974) to speculate that the eddies might be formed at the boundary of the basin as part of a shelfbreak circulation. Consistent with this idea, Spall et al. (2008) demonstrated that middepth, cold-core eddies are readily formed from baroclinic instability of a simulated shelfbreak jet when it advects winter water. These numerical results compared well with observations. The model current formed dipole pairs, but the shallow cyclones spun down rapidly because of contact with the (parameterized) ice. This is consistent with Ou and Gordon (1986), who investigated eddy spin down due to pack ice, and also with the fact that cyclones are mainly observed close to the Beaufort shelf (i.e., before they have a chance to spin down; A. Plueddemann and R. Krishfield 2007, personal communication). The formation mechanism of warm-core eddies is less well understood. The observations of D'Asaro (1988b) suggested that eddy generation occurs in both Barrow Canyon and Harold Canyon (D'Asaro 1988a). The model study of Watanabe and Hasumi (2009) implies that the source is the shelfbreak current during its seasonal warm phase, but the eddies so produced are significantly larger than indicated by the observations. The results to date suggest that horizontal processes such as eddy formation seem necessary to maintain the Pacific Summer Water temperature extremum in the interior basin, but uncertainty remains about the detailed mechanisms at work.

Recent observations have elucidated the structure and transport of the flow of Pacific Water along the shelf edge and slope of the Beaufort Sea, which is referred to here as the Western Arctic Shelfbreak Current. A mooring array maintained across the current revealed that the mean flow is eastward with a volume flux of  $0.13 \pm 0.08\text{ Sv}$  (Nikolopoulos et al. 2009). The fact that this value is less than a quarter of the estimated mean inflow through the Bering Strait suggested that much of the Pacific Water transport is quickly lost to the basin. Nikolopoulos et al. (2009) constructed seasonal composites of the shelfbreak current and found that in late winter and spring it is bottom intensified and transports Pacific Winter Water, whereas in late summer and early fall it is surface intensified and advects Alaskan Coastal Water. The winter water configuration of the current is baroclinically unstable in the absence of wind (Spall et al. 2008), whereas autumn and winter storms reverse the flow to the west and cause upwelling (Nikolopoulos et al. 2009; Pickart et al. 2011).

To date, the detailed structure, variability, and dynamics of the summer configuration of the Western

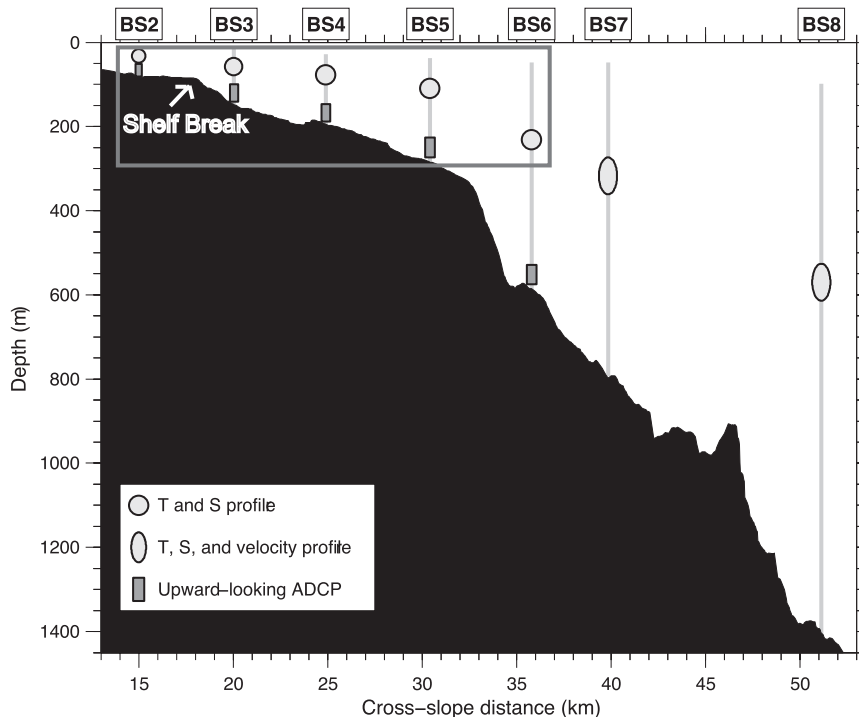


FIG. 2. The SBI mooring array at  $152^{\circ}\text{W}$  (after Spall et al. 2008). The different instruments are shown in the key (see text for details). The gray box shows the area of the array addressed in this study. The location of the shelfbreak is indicated (the coastline is 70 km inshore of the shelfbreak).

Arctic Shelfbreak Current have not been quantified, including the implications for eddy formation. This is the aim of the present study. Using the same mooring dataset considered by Nikolopoulos et al. (2009), we demonstrate that there are in fact two structurally and dynamically distinct configurations of the shelfbreak current advecting the two types of summer water noted above: Alaskan Coastal Water and Chukchi Summer Water. We investigate the timing, structure, stability, and energetics of the two current states, which provides insights regarding the fate of the warm waters advected by the current and their potential impact on the interior basin.

## 2. Data and methods

### a. Mooring array at $152^{\circ}\text{W}$

The western Arctic Shelf–Basin Interactions (SBI) program was designed to investigate the various physical, chemical, and biological mechanisms influencing the ecosystem at the interface between the shelf and slope in the Chukchi and Beaufort Seas (Grebmeier and Harvey 2005). As part of SBI, a mooring array was deployed at  $152^{\circ}\text{W}$  (yellow star in Fig. 1) across the shelfbreak downstream of Barrow Canyon primarily to investigate the Pacific Water flow along the Beaufort slope. Eight moorings were aligned roughly perpendicular to the local bathymetry.

Figure 2 shows a view of the mooring array in the vertical plane. (The most shoreward mooring failed in year 1 and is not considered in this study.) Each site contained a moored conductivity–temperature–depth (CTD) profiler to measure the hydrographic properties (the inner five sites employed coastal moored profilers sampling four times a day, and the outer two sites contained McLane moored profilers sampling twice a day). For velocity, upward-facing acoustic Doppler current profilers (ADCPs) were situated at the base of the inner five moorings, whereas acoustic current meters (ACMs) were used in conjunction with the moored profilers at the outer two sites. In the present study, we use only data from the five inner moorings, which measured temperature and salinity every 6 h and velocity hourly. The mooring array was deployed from 3 August 2002 to 9 September 2004, with an approximate 3-week gap (10 September–1 October 2003) when the mooring array was serviced. The moored profilers sampled only to 50-m water depth in order to remain a safe distance from ridging sea ice, whereas the ADCPs sampled in the lower 85% of the water column. This means that the near-surface temperature, salinity, and velocity were not recorded. Details of the instrumentation as well as estimates of the errors associated with the measurements are given in Nikolopoulos et al. (2009) for the velocity and in Spall et al. (2008) for the hydrography.

A local coordinate system was defined using the depth-averaged flow in conjunction with the principal axis variance ellipses (see Nikolopoulos et al. 2009). The positive  $x$  direction is essentially aligned along the bathymetry upstream of the array (i.e., east-southeast;  $125^\circ\text{T}$ ), and the positive  $y$  direction is north-northeast ( $35^\circ\text{T}$ ). The  $z$  direction is vertical (positive upward). In the following,  $x$  will be referred to as the alongstream direction and  $y$  will be referred to as the cross-stream direction. The tidal signal on the Beaufort slope is  $O(0.01 \text{ m s}^{-1})$ , which is weak compared to the mean velocities  $O(0.1 \text{ m s}^{-1})$ . To focus on mesoscale and longer time-scale variability, the velocities were low-pass filtered using a second-order low-pass Butterworth filter with a cutoff period of  $1/(36 \text{ h})$ .

Both the measured and derived variables from the array were gridded in the vertical plane using Laplacian-spline interpolation. This resulted in vertical sections of potential temperature, salinity, potential density, along-stream and cross-stream velocity, and the components of the potential vorticity at 6-h intervals. The standard grid has a horizontal spacing of 2 km and a vertical spacing of 10 m. To focus on the Pacific Water shelfbreak current, the grid is limited to 300 m in the vertical and 24 km in cross-stream distance, as shown by the gray box in Fig. 2.

### b. Shipboard sections

As noted above, the hydrographic measurements from the mooring array did not extend shallower than 50 m in the water column. To assess the impact of this gap in part of the analysis below, we made use of shipboard hydrographic and velocity data. In particular, three transects coincident with the mooring line at  $152^\circ\text{W}$  during the summer season provided synoptic full water column measurements of the shelfbreak current. The R/V *Palmer* completed CTD and vessel-mounted ADCP (VMADCP) sections on 19 July and 14 August 2003 (Swift and Codispoti 2003), when the shelfbreak current was advecting Alaskan Coastal Water. The USCGC *Healy* occupied a CTD and vessel-mounted ADCP section on 3 August 2009, during which time the shelfbreak current transported Chukchi Summer Water. These temperature, salinity, and velocity data were interpolated onto the same standard grid as the mooring data.

### c. 2-yr mean state

The mean hydrographic and velocity structure of the Western Arctic Shelfbreak Current over the 2-yr period of the mooring array is shown in Fig. 3. This is an extension of the presentation by Nikolopoulos et al. (2009), who used data from the first year only. The general features remain the same with the additional year of data. Water as cold as  $-1.4^\circ\text{C}$  corresponding to Pacific Winter Water is situated offshore between 100- and 200-m

depths. Pacific Summer Water is more prevalent inshore and above 100 m, where it results in mean temperatures as warm as  $-0.4^\circ\text{C}$ , even though it is only present for a comparatively short time of the year. The warm and salty Atlantic Water resides below the Pacific Winter Water (i.e., deeper than 200 m); the temperature maximum of the Atlantic layer is situated at roughly 400 m. In the region of the upper continental slope, the mean temperatures are moderate, even though the coldest winter water is found here during spring and early summer (Spall et al. 2008). This is because upwelling during autumn and winter often brings warm Atlantic Water up the slope, impacting the annual mean (Pickart et al. 2009).

In the mean density section, the isopycnals are sloping upward near the outer shelf and upper slope (the shelfbreak is situated near 85 m). This is consistent with the bottom intensification of the shelfbreak current as seen in the mean velocity section (velocity maximum of  $0.125 \text{ m s}^{-1}$ ). The full Ertel potential vorticity [see Eq. (1) below] is dominated by the stratification term. One sees that the Atlantic Water is characterized by very low stratification, above which lies a layer of stronger stratification within the halocline separating this water mass from the weakly stratified Pacific Winter Water above. The mean signature of Pacific Summer Water is characterized by enhanced stratification near 50-m depth.

## 3. Characteristics and timing of summer water masses

### a. Definition of summer water types

The Western Arctic Shelfbreak Current has a well-defined signature in the 2-yr mean as shown above. However, the mean represents the superposition of different configurations of the current occurring on mesoscale to seasonal time scales. To understand the mean and variability of the full boundary current system, the various dynamical processes at work need to be considered, sometimes individually. As such, the present study attempts to elucidate the summertime state of the Western Arctic Shelfbreak Current when it advects Pacific-origin waters that have been warmed in the Bering Sea and/or Chukchi Sea in early to midsummer before arriving at the array site. The first step, therefore, is to objectively define the two types of summer water noted above—the ACW and CSW—and identify when they are present at the array site.

Figure 4 shows the percentages of time during which different water masses are observed at the array. AW is defined here as  $\theta > -1^\circ\text{C}$  and  $S > 33$ , while PWW is defined as  $\theta < -1^\circ\text{C}$  and  $S > 33$ ; we do not attempt to distinguish different types of winter water, such as those discussed in Weingartner et al. (1998). AW and PWW were both present throughout the year with the PWW

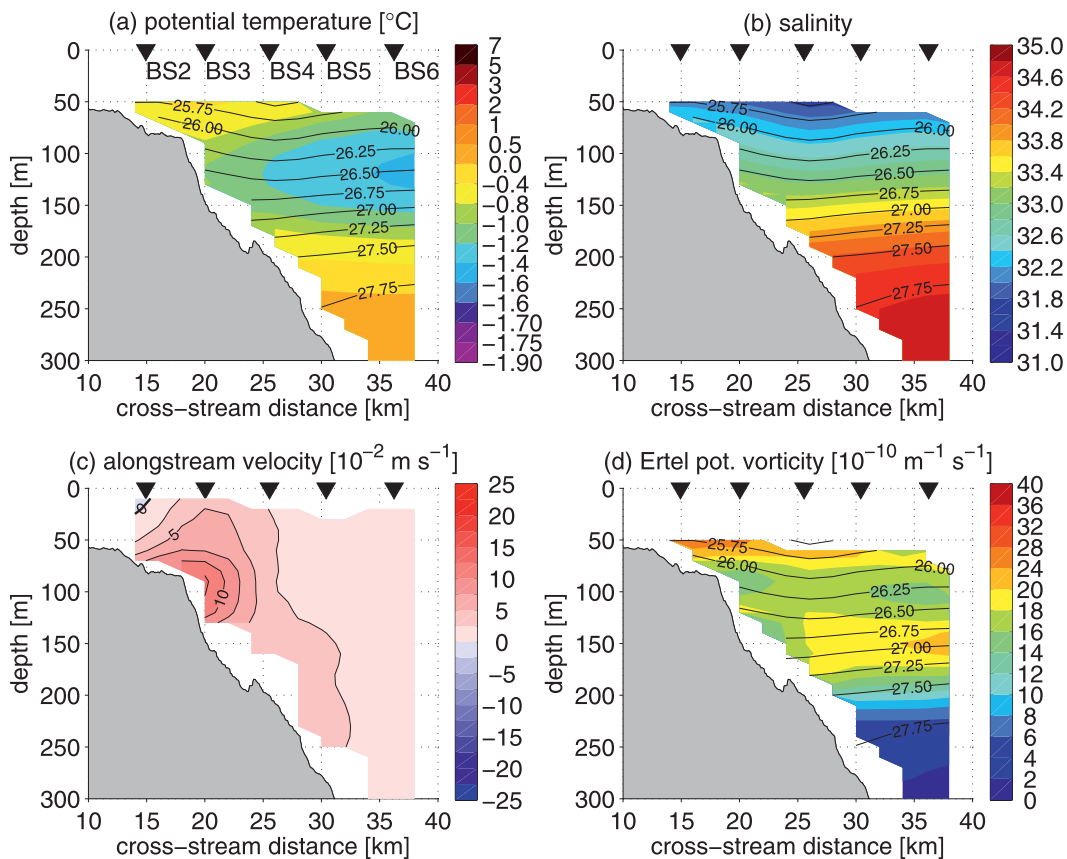


FIG. 3. Mean state of the Western Arctic Shelfbreak Current from 1 Aug 2002 to 1 Aug 2004. The colors show (a) potential temperature, (b) salinity, (c) alongstream velocity, and (d) Ertel potential vorticity, and the overlain contours show (a),(b),(d) potential density and (c) alongstream velocity. The five moorings BS2–BS6 used in the analysis are indicated by inverted black triangles and labeled in (a). The bathymetry is shaded gray.

overlying the AW typically at and below 200 m (except during periods of upwelling, when it can reach the upper slope and outer shelf). The PWW layer thickness varies both seasonally and synoptically, thinning considerably in summer.

Our study focuses on PSW broadly classified here as  $\theta > -1^{\circ}\text{C}$  and  $S > 33$ . It is present at the array intermittently from June through November each year. To distinguish between the two summer water types, the alongstream transport was calculated as a function of temperature and salinity. Within the summer water domain, there are two distinct mixing lines with the Pacific Winter Water: one containing an end member  $< 25 \text{ kg m}^{-3}$  and the other containing an end member  $> 25 \text{ kg m}^{-3}$  (Fig. 5). We interpret this to mean that the shelfbreak current at times advects predominantly very light water (ACW) mixing with PWW below and at other times advects less light water (CSW) mixing with PWW below. This distinction was used as an objective criterion for defining the two types of summer waters. For the shelfbreak current to

be in the ACW configuration, it is required to contain water lighter than  $25 \text{ kg m}^{-3}$  somewhere within the domain, whereas the CSW configuration consists only of water denser than  $25 \text{ kg m}^{-3}$ . This criterion may seem somewhat ad hoc, but it was motivated and supported by further evidence. For example, the sense of the thermal wind shear within the current varies in correspondence to summer water states defined as such.

In the mean, the shelfbreak current flows eastward, but as discussed in Pickart et al. (2009) the flow is often reversed to the west during autumn and winter upwelling storms. Inspection of the summer record also revealed westward flow reversals of the current (though less frequent). Comparing the summertime velocity record to wind data at Barrow Airport (Climate-Radar Data Inventories 2010), it was found that these current reversals were also due to upwelling favorable winds. Because the aim of the present study is to focus on the internal dynamics of the unforced eastward-flowing shelfbreak current, these wind-forced flow periods were excluded from our analysis.

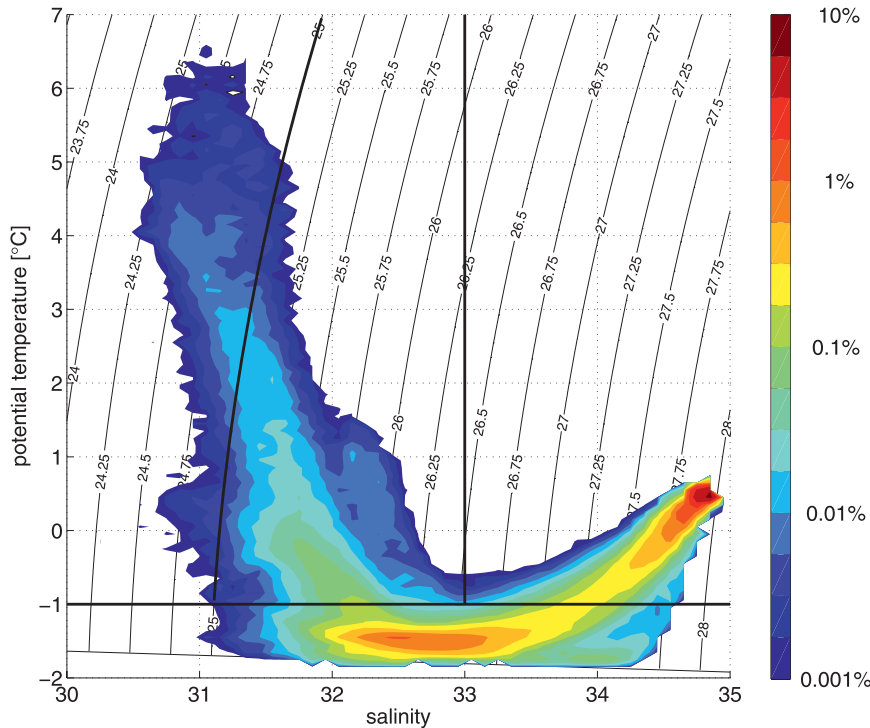


FIG. 4. Occurrence of water types as a function of temperature and salinity over the 2-yr deployment. Units are percentage of all measurements per  $0.1^{\circ}\text{C}$  and  $0.1$  salinity (note the logarithmic scale). The 33 line separating the Pacific from the Atlantic Water and the  $-1^{\circ}\text{C}$  line separating the winter water are indicated along with the  $25 \text{ kg m}^{-3}$  line separating the two summer water types.

### b. Temporal patterns of summer water

Both ACW and CSW were present in the shelfbreak jet for prolonged periods (Fig. 6). Note that by definition only one of the water types can be present at any one time, which is why occasionally the record alternates rapidly between ACW and CSW (when in fact there may have been a bit of both present in the current). The abrupt end of the record in early September 2003 is due to the mooring turnaround. The mooring array was operational again at the beginning of October 2003, and, although there were small quantities of water fulfilling CSW criteria present into mid-January 2004, comparison to the velocity fields showed that this water was situated shallower than the bottom-intensified shelfbreak jet. Therefore, this time period was excluded from consideration. Also, the data from early August 2004 onward are heavily biased by the fact that mooring BS5 stopped functioning, making it impossible to construct meaningful vertical sections. This time period was excluded as well. In the analysis below, we ignore the short “intrusion events” of one of the water masses during periods of sustained presence of the other. As mentioned above, we also removed periods of current reversals. The resulting time periods of the unforced shelfbreak current accounted for more than 60% of the

summer record in 2002 and 2004 and more than 90% in 2003. The divisions between the ACW and CSW states of the shelfbreak jet are denoted by the red and green symbols, respectively, in Fig. 6.

### c. Seasonal variability

Although there is significant interannual variability of the shelfbreak current (see below), a typical seasonal progression of the two summer states of the jet emerges based on the 26 months of mooring data. In particular, the summer season (i.e., when warm water is present at the array site) begins with the arrival of CSW, followed 2–4 weeks later by warmer, lighter ACW. Then, in late summer/early fall, CSW appears again. Although one may wonder if this sequence is due to our water mass definition equating very light water with ACW, below we demonstrate that these two states of the summertime shelfbreak jet are dynamically distinct as well.

### d. Interannual variability

As seen in Fig. 6, the arrival of summer water in 2002 (17 August) was significantly later than in 2003 (5 July) and 2004 (23 June). Note that this discrepancy was not due to the timing of the mooring array deployment in 2002,

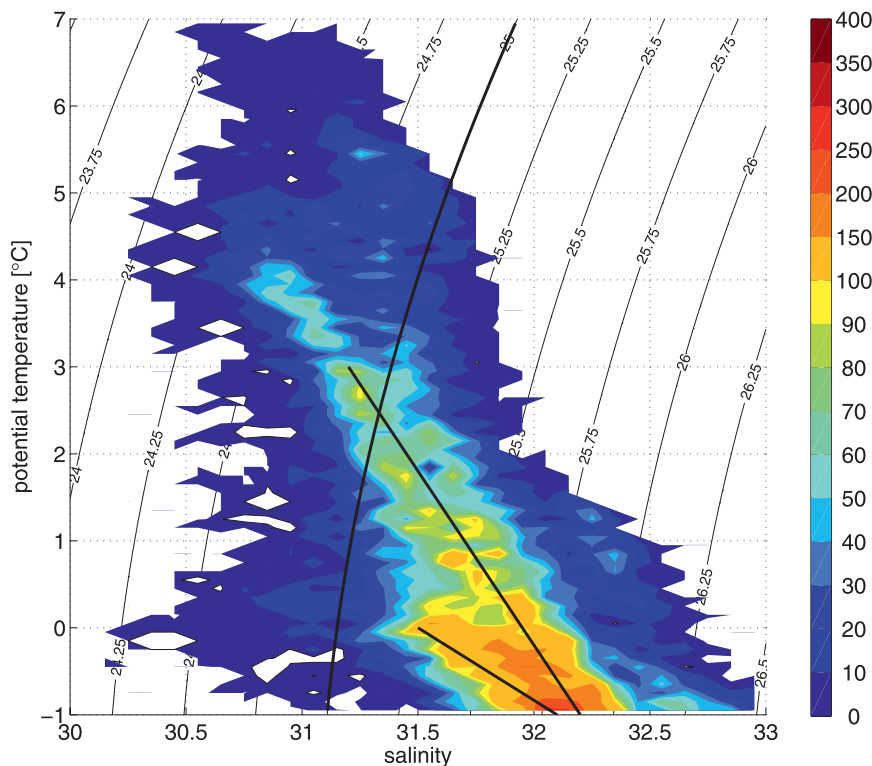


FIG. 5. Transport within the summer water domain ( $S < 33$  and  $\theta > -1^\circ\text{C}$ ) over the 2-yr deployment as a function of temperature and salinity. Units are  $\text{m}^3 \text{s}^{-1}$  per  $0.1^\circ\text{C}$  and  $0.1$  salinity (note the nonlinear scale). The  $25 \text{ kg m}^{-3}$  line separating the two summer water types is highlighted along with the major mixing lines between PWW and ACW and between PWW and CSW.

because the instruments did not detect the presence of summer water during the first 2 weeks of the deployment. One possible explanation for this significant delay is that warm water did not enter Bering Strait until later in the year in 2002. To investigate this, we considered data from mooring A4 in Bering Strait (e.g., Woodgate and Aagaard 2005). The time when the near-bottom potential temperature at A4 first exceeded  $-1^\circ\text{C}$  was used as an indication for the arrival of summer water at the strait. For all three summers in question (2002–04), the arrival times fell between 10 and 17 May (i.e., within a one-week period). Hence, this cannot explain the delay at the Beaufort slope array site.

A second possibility is that the flow speed in Bering Strait was weaker in summer 2002 and hence the water took longer to progress to the Beaufort Sea. As a proxy for this, we integrated the near-bottom velocity in time (using data from a point current meter at 40-m depth until 26 June 2002 and the lowest ADCP bin at 34-m depth thereafter). For the month-long period after the arrival of summer water in the strait, the cumulative displacement of water parcels was 1400 and 1600 km in 2003 and 2004 respectively, whereas it was 1000 km in 2002. Although the distance is shorter in 2002, it is nonetheless the same

order of magnitude as the distance from Bering Strait to the mooring array (1150 km). Therefore, we conclude that conditions in Bering Strait alone cannot account for the late arrival of the summer water in 2002 at the array site. A preliminary analysis of the large-scale winds over the Chukchi Sea from the National Centers for Environmental Prediction (NCEP) reanalysis (Kalnay et al. 1996) revealed no obvious interannual change explaining the delay (for a discussion about the quality of wind velocities from atmospheric reanalyses in the region, see Pickart et al. 2011). Instead, oceanic processes in the Chukchi Sea and/or in Barrow Canyon were likely responsible for the delay.

#### 4. Summer water current configurations and their transports

##### a. Alaskan Coastal Water configuration

The configuration of the Western Arctic Shelfbreak Current when it advects ACW was investigated by constructing composite average vertical sections of the flow for both 2002 and 2003, corresponding to the ACW realizations identified in Fig. 6. For all properties, we computed the mean and standard error at each grid point

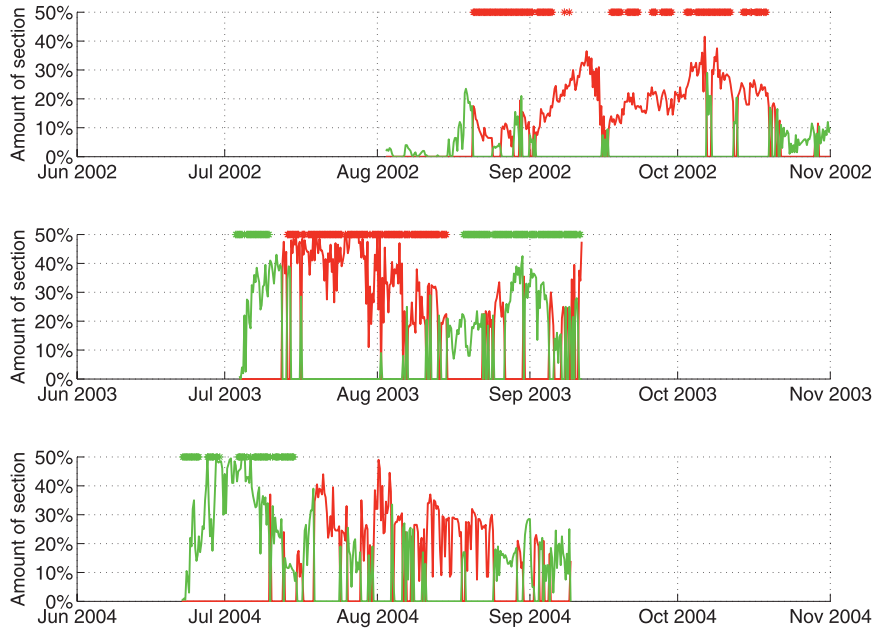


FIG. 6. Amount of area within the gray box of Fig. 2 occupied by ACW (red curve) and CSW (green curve) as a function of time. The time periods that have been considered for the composite averages of the boundary current are indicated by the symbols at the top of each row: ACW (red) and CSW (green). The record termination on 10 Sep 2003 is due to the mooring turnaround that lasted until 1 Oct 2003.

of the standard section. The mean structure of the current in 2002 is shown in Fig. 7. There are three water masses present in the section: ACW, PWW (or more precisely remnant winter water), and AW (at depths greater than 200 m). The PWW is located between 80 and 200 m with temperatures as low as  $-1.6^{\circ}\text{C}$  (i.e., less than  $0.2^{\circ}\text{C}$  above the freezing point). As noted above, PWW was present somewhere in the water column during the entire record.

In the composite mean section, the ACW occupies the region inshore of 30 km and above 100 m with water as fresh as 31 and as warm as  $5^{\circ}\text{C}$ . The hydrographic data coverage does not extend inshore of 18 km and above 50 m, but the fact that the measured temperature maximum and salinity minimum are found on the edge of the data coverage suggests that there is warmer and fresher water inshore and at shallower depths. This is usually the case in shipboard CTD sections. For example, the R/V *Palmer* occupied a transect across the array line in summer 2003, which provides an opportunity to compare such a shipboard section with a synoptic snapshot from the array. As seen in Fig. 8, both the qualitative and quantitative agreement is very good in the region of overlap. However, the minimum salinity in the shipboard section in the near-surface water is lower by a value of 2 than that measured near 50 m by the moorings (interestingly, the maximum temperatures are comparable in the two sections).

In the vicinity of the shelfbreak at 18 km, the mean isopycnals in Fig. 7 slope upward in the offshore direction. By thermal wind, this implies an increase in the alongstream velocity toward the surface. This is consistent with the alongstream velocity measured directly from the ADCPs. The mean current is surface intensified and clearly trapped to the shelfbreak. However, there is strong eastward flow as far as 20 km offshore of the shelfbreak. The standard error in velocity (not shown) is smaller than the mean everywhere above 200 m.

The Ertel potential vorticity  $\Pi$  is defined as

$$\Pi = \frac{-f}{\rho_0} \frac{\partial \sigma_{\theta}}{\partial z} + \frac{1}{\rho_0} \frac{\partial u}{\partial y} \frac{\partial \sigma_{\theta}}{\partial z} - \frac{1}{\rho_0} \frac{\partial u}{\partial z} \frac{\partial \sigma_{\theta}}{\partial y}, \quad (1)$$

where the three terms correspond to the stretching vorticity, relative vorticity, and tilting vorticity (see, e.g., Hall 1994). Instantaneously, the relative vorticity can be as large as the stretching vorticity, indicating that the flow is highly energetic and variable. However, in the composite time mean of Fig. 7, the potential vorticity is dominated by the stretching term. The core of the shelfbreak current is strongly stratified, which is due to the fact that ACW originates from river runoff in the Gulf of Alaska (Weingartner et al. 2005). The second region of enhanced stratification corresponds to the interface between PWW and the AW near a depth of

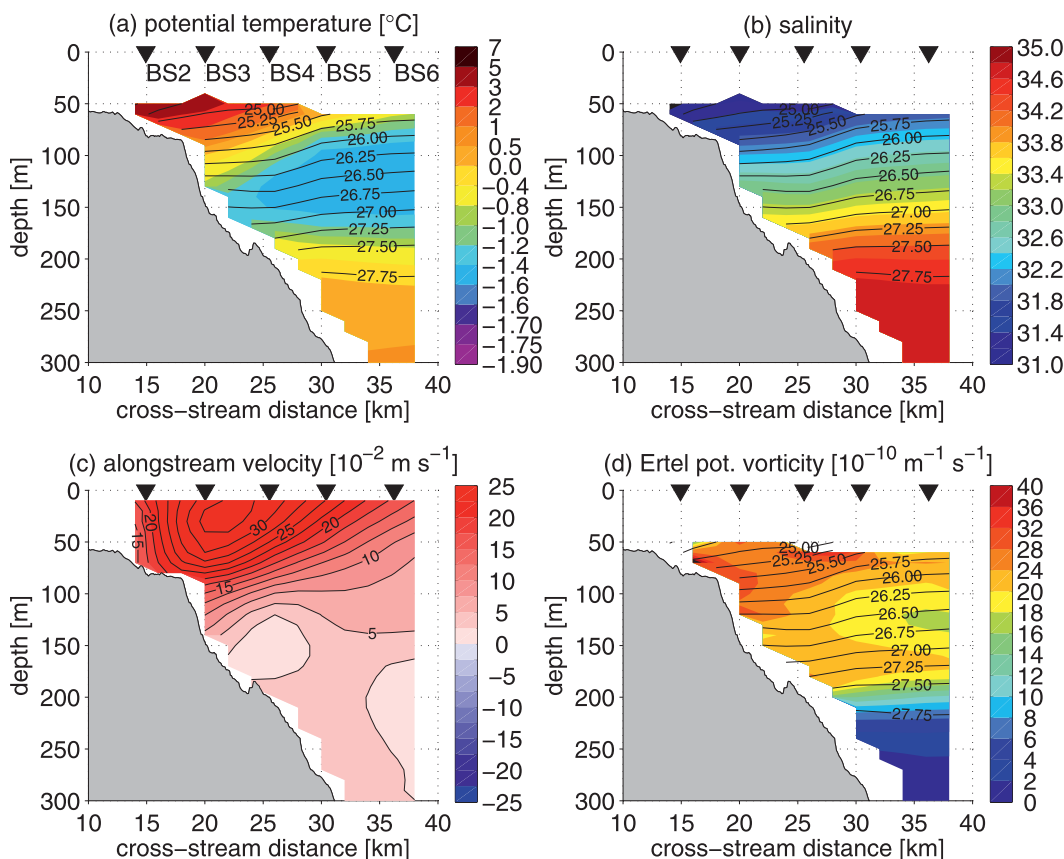


FIG. 7. Mean state of the Western Arctic Shelfbreak Current advecting ACW in 2002. Quantities plotted are as in Fig. 3.

180 m (see also Nikolopoulos et al. 2009). Note that near 70-m depth,  $\Pi$  increases in the offshore direction, whereas the opposite is true near 130 m. This reversal of the horizontal mean potential vorticity gradient is a necessary condition for baroclinic instability of the shelfbreak current. Overall, the ACW configuration can be described as a surface-intensified shelfbreak current of strongly stratified warm water.

Although not presented here, the ACW composite for 2003 agrees well with the above findings. However, in 2003 the jet transported more buoyant water than in 2002, resulting in somewhat more pronounced lateral property gradients across the shelfbreak current.

#### b. Chukchi Summer Water configuration

The CSW configuration of the Western Arctic Shelfbreak Current was well sampled in the summer of 2003 for about a month, whereas the record in 2004 was shorter and more intermittent because of instrument failures. Hence we present the 2003 composite sections in Fig. 9, although the 2004 means are qualitatively similar. Again, there are three distinct water masses present in the section

with the CSW overlying remnant PWW and AW. In this case, the temperature of the summer water exceeds  $1^{\circ}\text{C}$  and the salinity is as low as 31.6.

In contrast to the ACW configuration, the current here is bottom-intensified with eastward flow  $> 0.2 \text{ m s}^{-1}$  in the mean. The isopycnals slope downward in the offshore direction just offshore of the shelfbreak and just above the core of the bottom-intensified flow (between 20 and 25 km). By thermal wind, the isopycnal slope implies increasing flow with depth consistent with the observed flow field. Again, the current is trapped to the shelfbreak (although there is a hint of surface-intensified flow in the middle of the section). Also, in contrast to the ACW state, the CSW is weakly stratified. The potential vorticity structure of the CSW composite mean is such that there is a minimum in the core of the current near 100 m with increasing values in the offshore direction. Deeper than this, the sense of the lateral gradient of  $\Pi$  is reversed (near 180 m at the interface between the PWW and AW). Hence, the potential vorticity structure also fulfills the necessary condition for baroclinic instability. Overall, the CSW configuration can be described as

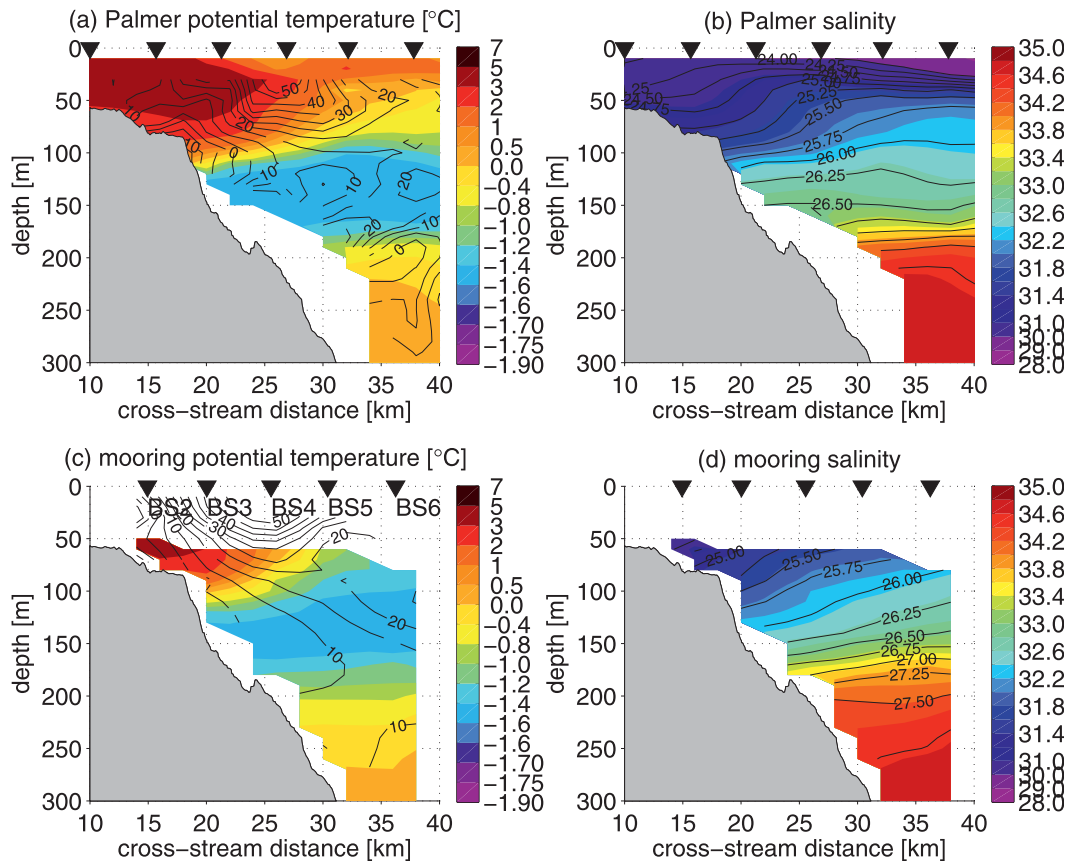


FIG. 8. Synoptic snapshot of the Western Arctic Shelfbreak Current advecting ACW in 2003. Data from the mooring array are presented at 0600 UTC 14 Aug 2003. The R/V *Palmer* performed an offshore to inshore CTD and vessel-mounted ADCP section on the same day and was at cross-stream distance 27 km at 0600 UTC. (a),(b) Data from R/V *Palmer* and (c),(d) data from the mooring array. (a),(c) Potential temperature in color overlain by alongstream velocity and (b),(d) salinity in color overlain by potential density. Note the added contour intervals for salinity between 28 and 31. Flux estimates of volume, freshwater, and heat for an extrapolation as described in the text agree to within 25% of each other: 0.73 Sv, 61 mSv, and  $7.8 \times 10^{12} \text{ J s}^{-1}$  from R/V *Palmer* and 0.84 Sv, 49 mSv, and  $6.2 \times 10^{12} \text{ J s}^{-1}$  from the mooring array.

a bottom-intensified shelfbreak current of weakly stratified warm water.

### c. Transports

We now present the fluxes of mass, heat, and salt for the different states of the shelfbreak current. For completeness, in addition to the ACW and CSW configurations described above, we also consider the PWW case investigated by Spall et al. (2008). This corresponds to the time period April–June 2003 when the coldest (most recently ventilated) winter water passed by the array. The composite vertical sections for this configuration are shown in Fig. 10. As in the CSW case, the current is weakly stratified, bottom intensified, and trapped to the shelfbreak. However, the water it advects has temperatures near the freezing point. As discussed in Spall et al. (2008), this configuration of the current is baroclinically unstable and forms cold-core, anticyclonic eddies.

In terms of data coverage, the ADCP measurements in the mooring array were able to adequately span the shelfbreak current, enabling accurate estimates of volume flux for all three configurations (ACW, CSW, and PWW). However, the CTD profilers did not measure the upper 50 m of the water column. As noted above, Fig. 8 illustrates the impact of this data gap for the ACW case. As seen, the water column continues to become fresher and (slightly) warmer upward of where it was sampled by the moorings. As a simple attempt to fill this gap, we performed a constant extrapolation of the temperature and salinity fields to the surface, realizing that this will lead to an underestimate of the heat and freshwater fluxes. To assess the magnitude of this bias, we compare transports computed from the mooring array (using the constant extrapolation) and from the ship section (see Fig. 8). This shows that in the ACW case the mooring-based estimates of heat and freshwater transport account for at least 70%

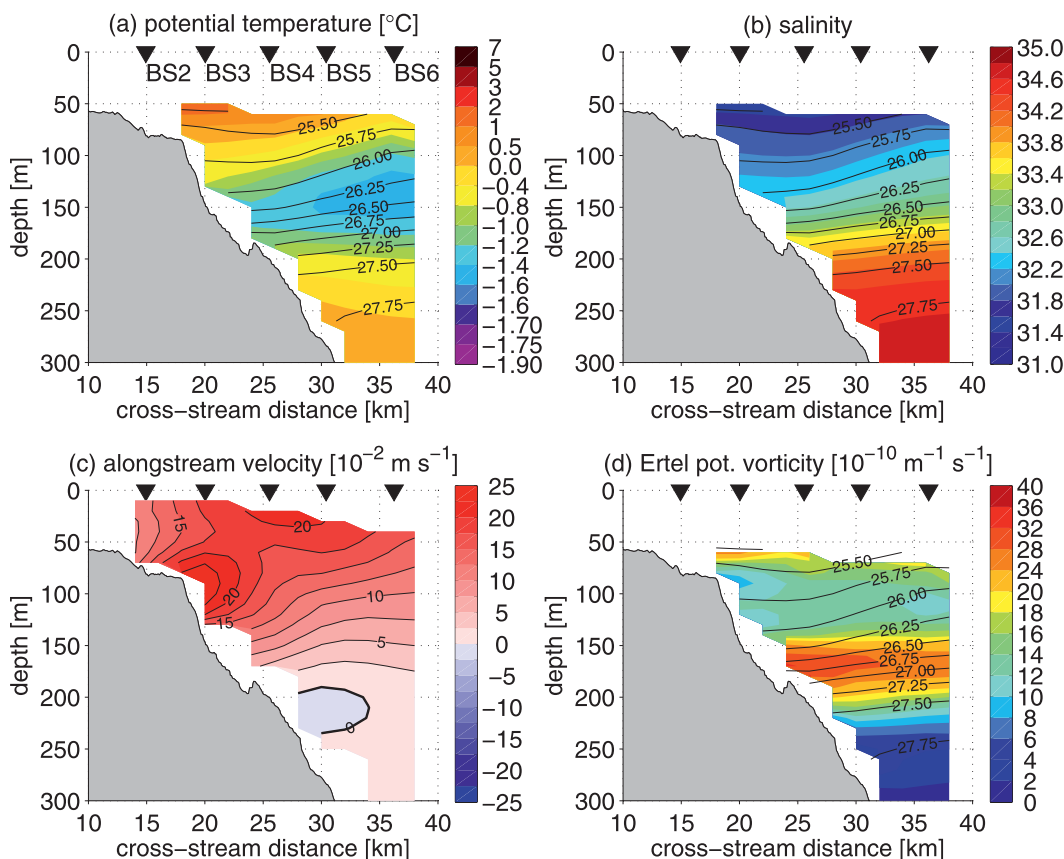


FIG. 9. Mean state of the Western Arctic Shelfbreak Current advecting CSW in 2003. Quantities plotted are as in Fig. 3.

of the ship-based estimates. For the CSW and the PWW case, the velocity maximum is within the hydrographic coverage, and therefore the heat and freshwater flux estimates are less biased.

Because there is a nonzero net volume flux across the array, we cannot compute formal estimates of freshwater and heat flux divergence (for a discussion, see Schauer and Beszczynska-Möller 2009). Following earlier studies, we chose a reference salinity of 34.8. This is the mean salinity of Atlantic Water in the Arctic Ocean and therefore provides a freshwater flux that is relevant for the maintenance of the halocline. For temperature, we chose a reference value of  $-1.91^{\circ}\text{C}$ , which is the freezing point at the reference salinity and thus reflects the heat available for melting sea ice.

The fluxes of mass, heat, and freshwater in the upper 300 m of the water column, including random (but not systematic) errors, are given in Table 1, which also presents data from other studies for comparison. The reader should keep in mind that these values are for periods when the jet was not forced by easterly (upwelling favorable) winds. Because the shelfbreak current reverses during those events (Nikolopoulos et al. 2009), the transports

become negative and the sum of unforced and reversed transports will be smaller than for the unforced states by themselves. The volume flux during all three (unforced) configurations is  $O(0.5 \text{ Sv})$ , with slightly larger values for the ACW state. Nikolopoulos et al. (2009) distinguished between the transport of Pacific Water and Atlantic Water using stratification to determine the interface between the two water masses. We made no such attempt here. However, because the transport of Atlantic Water within the array shallower than 300 m is quite small, we conclude that the transports presented in Table 1 are reasonable proxies for Pacific Water transport. The fluxes for the ACW state during 2003 were roughly 30% stronger than for 2002.

The year-long (including all different wind regimes) volume, freshwater, and heat fluxes are on the order of  $0.2 \text{ Sv}$ ,  $10 \text{ mSv}$ , and  $1.5 \times 10^{12} \text{ J s}^{-1}$ , respectively, with the second year being somewhat stronger than the first. These fluxes are between 10% and 20% of the corresponding fluxes of Pacific Water through Bering Strait (Table 1). The heat fluxed eastward past  $152^{\circ}\text{W}$  would be able to melt roughly  $160\,000 \text{ km}^2$  of 1-m-thick sea ice. Both the heat and freshwater fluxes during the ACW periods are

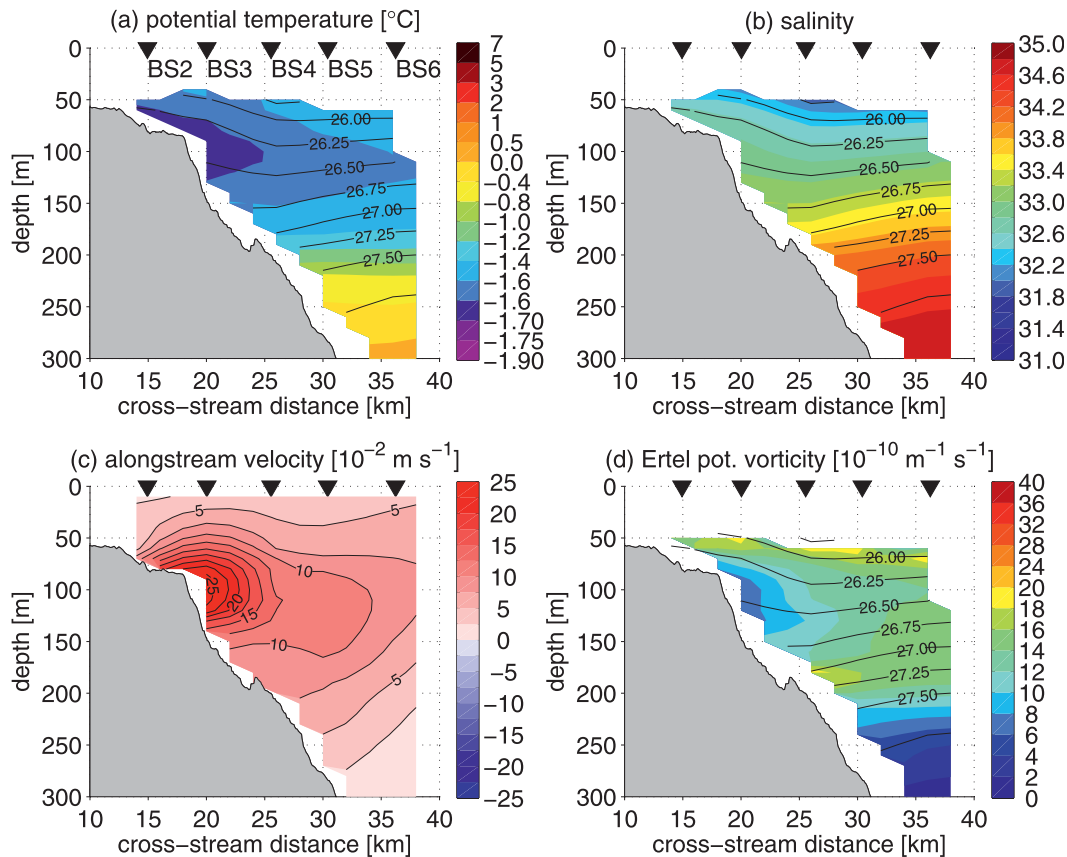


FIG. 10. Mean state of the Western Arctic Shelfbreak Current advecting PWW in 2003 (after Spall et al. 2008). Quantities plotted are as in Fig. 3.

stronger than during the CSW periods, mainly because the current is stronger and the salinity and temperature anomalies are larger. Keep in mind that, because of the constant extrapolation above 50 m for the hydrographic variables, the ACW case underestimates the freshwater and heat transports more so than the CSW case.

Despite the relatively large error bars in Table 1, it is clear that a significant portion of the Pacific Water entering the Chukchi Sea through Bering Strait does not end up in the shelfbreak current east of Point Barrow (consistent with the results of Nikolopoulos et al. 2009). The year-long Bering Strait flux estimates in Table 1 (R. Woodgate 2010, personal communication) include the contribution due to the Alaskan Coastal Current, which is 2–5 times larger than the (year long) transport associated with ACW at 152°W determined here. This is mainly because the Alaskan Coastal Current is present in Bering Strait for a longer duration than ACW is observed at the mooring array. This suggests that there are times when the Alaskan Coastal Current reaches the Beaufort shelf with little change in transport (note the large transport of the ACW composite vertical section) but that

there are also significant periods when the current is diverted from the Beaufort shelf.

### 5. Energetics and downstream fate of the shelfbreak current

#### a. Energetics

As noted earlier, eddies with ACW and CSW signatures have been observed in the interior Beaufort Sea. It is natural to hypothesize that instability of the summertime shelfbreak jet may lead to the formation of these eddies. We now investigate this hypothesis by analyzing the energetics of the observed states of the jet using a similar approach as Brink et al. (2007).

Following a fluid parcel, the change of the total energy of the mean current is

$$D(P + K)/Dt = -C - T - S \pm \text{pressure work} \\ \pm \text{wind work} - \text{bottom friction}, \quad (2)$$

where  $D/Dt$  is the advective derivative acting on the sum of the mean available potential energy,

TABLE 1. Fluxes during different configurations of the shelfbreak current compared to Bering Strait. The duration is the length of time over which the estimate was made for each case. The freshwater flux is relative to 34.8, and the heat flux is relative to  $-1.91^{\circ}\text{C}$ . Standard errors take into account the cross correlation between the time series at the individual grid points. The four summer water time periods are identified in section 3. PWW2003 is the PWW period in spring 2003 discussed by Spall et al. (2008). The fluxes for these cases, plus the first-year, second-year, and 2-yr mean, are based on the gray box in Fig. 2. For comparison, the first-year fluxes at  $152^{\circ}\text{W}$  from Nikolopoulos et al. (2009) are included. These are based on the entire array down to 800 m, where the PW and AW contributions have been distinguished. The Bering Strait fluxes are primarily based on the single mooring A3 in the strait (R. Woodgate 2010, personal communication; Woodgate et al. 2010). The freshwater fluxes include the additional contribution of the ACC and stratification. The heat fluxes include a 10-m-thick layer of water at the same temperature as the satellite-derived sea surface temperature. The fluxes resulting from the ACC (present for 3–5 months per year) alone are also presented.

	Duration (days)	Volume flux (Sv)	Freshwater flux (mSv)	Heat flux ( $10^{12} \text{ J s}^{-1}$ )
ACW2002	35	$0.60 \pm 0.12$	$44 \pm 9$	$6.4 \pm 1.4$
ACW2003	29	$0.87 \pm 0.17$	$61 \pm 10$	$10.1 \pm 1.7$
CSW2003	29	$0.57 \pm 0.11$	$39 \pm 7$	$3.7 \pm 0.8$
CSW2004	15	$0.62 \pm 0.13$	$42 \pm 7$	$4.2 \pm 1.2$
PWW2003	57	$0.44 \pm 0.07$	$21 \pm 4$	$0.8 \pm 0.2$
First year (August 2002–July 2003)	365	$0.16 \pm 0.05$	$9 \pm 3$	$1.3 \pm 0.4$
Second year (August 2003–July 2004)	366	$0.20 \pm 0.05$	$13 \pm 3$	$1.6 \pm 0.3$
2 yr (August 2002–July 2004)	731	$0.18 \pm 0.03$	$11 \pm 2$	$1.5 \pm 0.3$
First-year PW (August 2002–July 2003)	365	$0.13 \pm 0.08$	—	—
First-year AW (August 2002–July 2003)	365	$0.047 \pm 0.026$	—	—
Bering Strait 2002 (January–December 2002)	365	$0.82 \pm 0.10$	$(51 + 29) \pm 10$	$11 \pm 3$
Bering Strait 2003 (January–December 2003)	365	$0.89 \pm 0.10$	$(64 + 29) \pm 13$	$12 \pm 3$
Bering Strait ACC (2000–03)	90–150	$0.24 \pm 0.07$	$32 \pm 13$	$10 \pm 3$

$$P = -\frac{1}{2}g\bar{\rho}^2(\rho_{0z})^{-1}, \quad (3)$$

and mean kinetic energy,

$$K = \frac{1}{2}\rho_0(\bar{u}^2 + \bar{v}^2). \quad (4)$$

Here,  $\rho_0(z)$  is the mean density profile outside of the shelfbreak current and  $\rho(x, y, z, t)$  is the deviation from that mean density profile. The total energy of the system changes over time due to baroclinic mean-to-eddy conversion,

$$C = g\bar{\rho}'v'\frac{\bar{\rho}_y}{\bar{\rho}_z} = -g\bar{\rho}'v'\frac{\partial z}{\partial y}, \quad (5)$$

where  $\partial z/\partial y$  is the slope of the isopycnals, and barotropic mean-to-eddy conversion,

$$T = -\rho_0\overline{u'v'}\bar{u}_y, \quad (6)$$

as well as shear mean-to-eddy conversion  $S$ . In addition, there is pressure work, wind forcing, and bottom friction. All quantities have been decomposed into their time mean (e.g.,  $\bar{u}$ ) and the time-dependent deviation from the mean (e.g.,  $u'$ ). No observations of the typical scale of alongstream variations  $L^x$  are available, but the topographic control suggests that  $L^x$  is much larger than the

typical scale of cross-stream variations  $L^y$ . Assuming that variations in the alongstream direction are advected past the array by the alongstream velocity, temporal variability at the array can be transformed into alongstream variability, which confirms the assumption that  $L^x \gg L^y$ . This assumption has been used to arrive at the simplified expressions for  $C$  and  $T$  above. Additionally, assuming that the continuity equation is balanced in the horizontal to lowest order (as in quasigeostrophic theory), the vertical velocities are much smaller than the horizontal velocities times the aspect ratio. This means that the shear mean-to-eddy conversion term  $S$  is much smaller than  $T$ ; hence, we neglect it here. The effects of large-scale pressure gradients, wind forcing, and friction are not included explicitly here, but their effects are discussed qualitatively below.

With the exception of  $\rho_0(z)$  (the background profile of density offshore of where the shelfbreak current deforms the isopycnals), all of the necessary information is available from the mooring data to compute the simplified expressions for  $P$ ,  $K$ ,  $C$ , and  $T$  given above. Because Figs. 7, 9, and 10 show that the shelfbreak current is situated inshore of mooring BS6, we have computed a mean density profile  $\rho_0$  from the outer two moorings BS7 and BS8. The terms in the energy equation plotted in the vertical plane are shown in Figs. 11–13 for the three states of the current (ACW, CSW, and PWW). These quantities have also been summed over the full cross section and—taking into account the cross correlation of the time series at each grid point—the standard errors of the sums

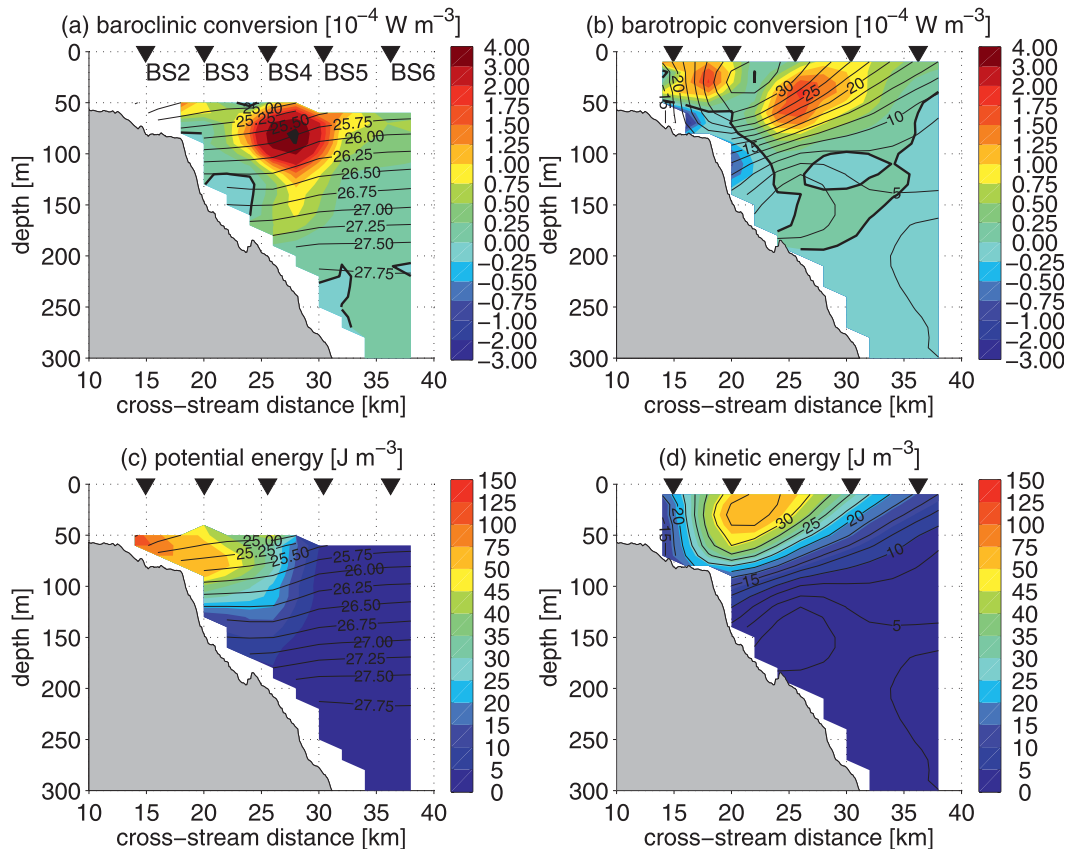


FIG. 11. Energetics of the Western Arctic Shelfbreak Current advecting ACW in 2002. The colors show (a) baroclinic mean-to-eddy conversion, (b) barotropic mean-to-eddy conversion, (c) available potential energy, and (d) kinetic energy. The overlain contours show (a),(c) potential density and (b),(d) alongstream velocity.

have been calculated. These sums are given in Table 2 for each of the time periods considered.

For the ACW in 2002 (Fig. 11), the baroclinic conversion from mean to eddy available potential energy is greatest in the region where the isopycnals slope upward most strongly. The barotropic conversion from mean to eddy kinetic energy shows two distinct maxima at the inshore and offshore edge of the mean current. The sums of these two conversion terms are statistically different from zero. The baroclinic conversion is  $180 \pm 78 \text{ W m}^{-1}$ , whereas the barotropic conversion is  $102 \pm 34 \text{ W m}^{-1}$  (roughly a factor of 2 smaller). As noted above, the potential vorticity structure of the ACW state in 2002 satisfies the necessary condition for baroclinic instability. Together with the strong baroclinic conversion, this implies that the jet is baroclinically unstable. Although the current in this state also satisfies the two necessary conditions (Rayleigh's and Fjørtoft's criteria) for barotropic instability, these are relevant for a beta plane. As discussed in Spall and Pedlosky (2008), when topographic effects are taken into account these conditions are no longer adequate. Hence, we are unable to unequivocally

rely on theory to make the case that barotropic instability is active. However, the two regions of strong barotropic conversion computed from the data are located where the horizontal shear in the mean velocity is largest (Fig. 11), which is as expected for classical barotropic instability. Thus, these results suggest that the ACW configuration of the Western Arctic Shelfbreak Current in 2002 was subject to a mixed instability.

Not surprisingly, the spatial distribution of mean kinetic energy for the ACW state in 2002 corresponds closely to the mean alongstream velocity and is well captured by the array. However, the mean available potential energy is largest near the edge of the sampled region. To assess the impact of this data gap, we computed the available potential energy and kinetic energy for two summertime CTD transects of the shelfbreak current during the ACW phase (Fig. 8 shows the hydrography during the second crossing). During the two crossings, the total energy as computed from the moorings accounted for 102% and 76%, respectively, of the energy computed using the ship sections. Although the latter are synoptic snapshots that are expected to differ from longer-term means such as

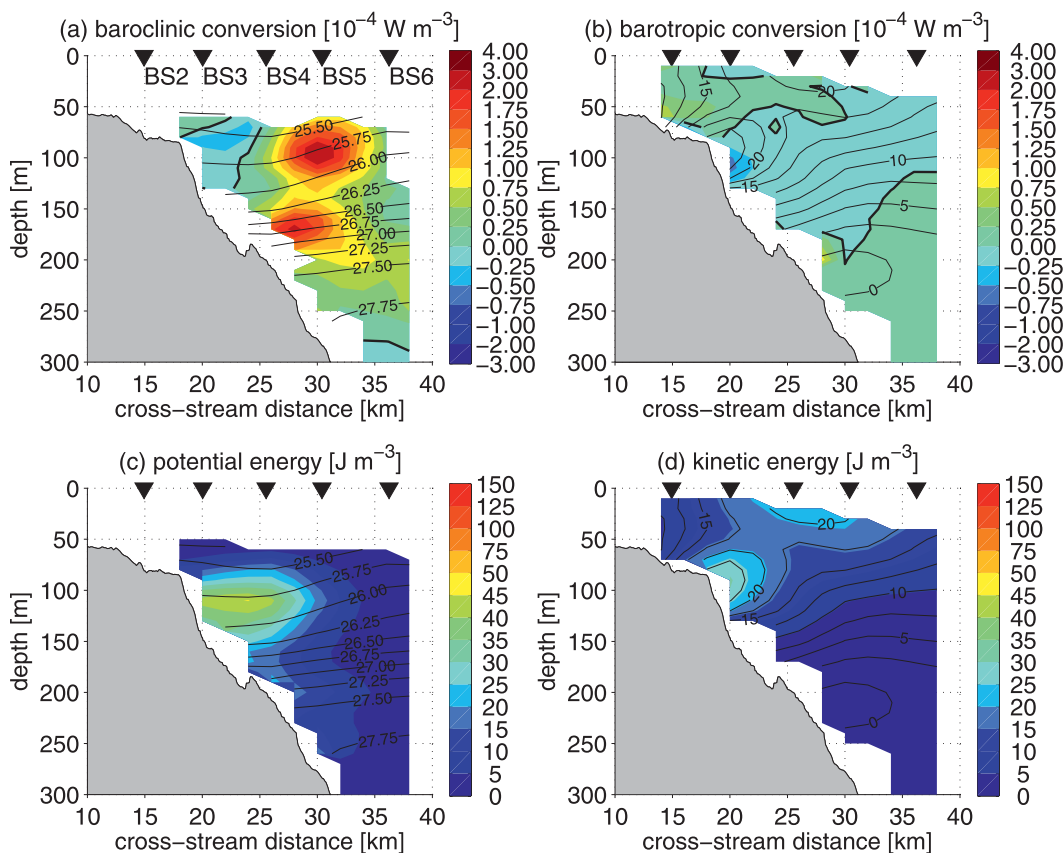


FIG. 12. Energetics of the Western Arctic Shelfbreak Current advecting CSW in 2003. Quantities plotted are as in Fig. 11.

presented in Fig. 11, it suggests that the energy estimates from the moorings account for significantly more than half of the total energy. This is mainly because, although the top 50 m contains very buoyant water, this buoyant water is not completely confined within the shelfbreak current and is therefore not associated with strong horizontal density gradients.

Because the mean hydrographic and velocity structure of the ACW in 2003 is qualitatively similar to 2002, it is expected that the energetics would be similar as well. As shown in Table 2, both the baroclinic and barotropic conversion are again positive; however, the baroclinic conversion is not statistically different from zero.

The energetics of the CSW configuration of the shelfbreak current in 2003 are shown in Fig. 12. As in the ACW case, there is strong baroclinic conversion in the region where the isopycnals are sloping most strongly upward and the sum (see Table 2) is significantly positive. By contrast, the barotropic conversion in this state has no pronounced structure and its sum is not statistically different from zero. This is consistent with the fact that this configuration also does not fulfill Rayleigh's necessary criterion for barotropic instability on a beta plane.

Accordingly, we conclude that the CSW configuration of the shelfbreak current is baroclinically unstable. We note that the estimate of the potential energy for this case is more robust than for the ACW case because the bias due to the data gap is smaller. With a shorter and more intermittent record for CSW in 2004, the baroclinic conversion is marginally positive and the barotropic conversion is in fact negative (implying some energy transfer into the mean kinetic energy). Although quantitatively not as robust as in 2003, this still supports the conclusion that the CSW configuration is baroclinically unstable.

Spall et al. (2008) concluded that the PWW configuration in 2003 was baroclinically unstable. For comparison purposes, the energy conversions for that case are included in Table 2 and shown in Fig. 13. Estimates of the mean kinetic and available potential energy (computed here) are added. As noted by Spall et al. (2008), the net barotropic conversion is small and the baroclinic conversion is positive. However, the magnitude of the baroclinic conversion ( $55 \pm 51 \text{ W m}^{-1}$ ) is only about 25% of that for the ACW state in 2002 and the CSW state in 2003. This means that the PWW configuration in 2003 is less

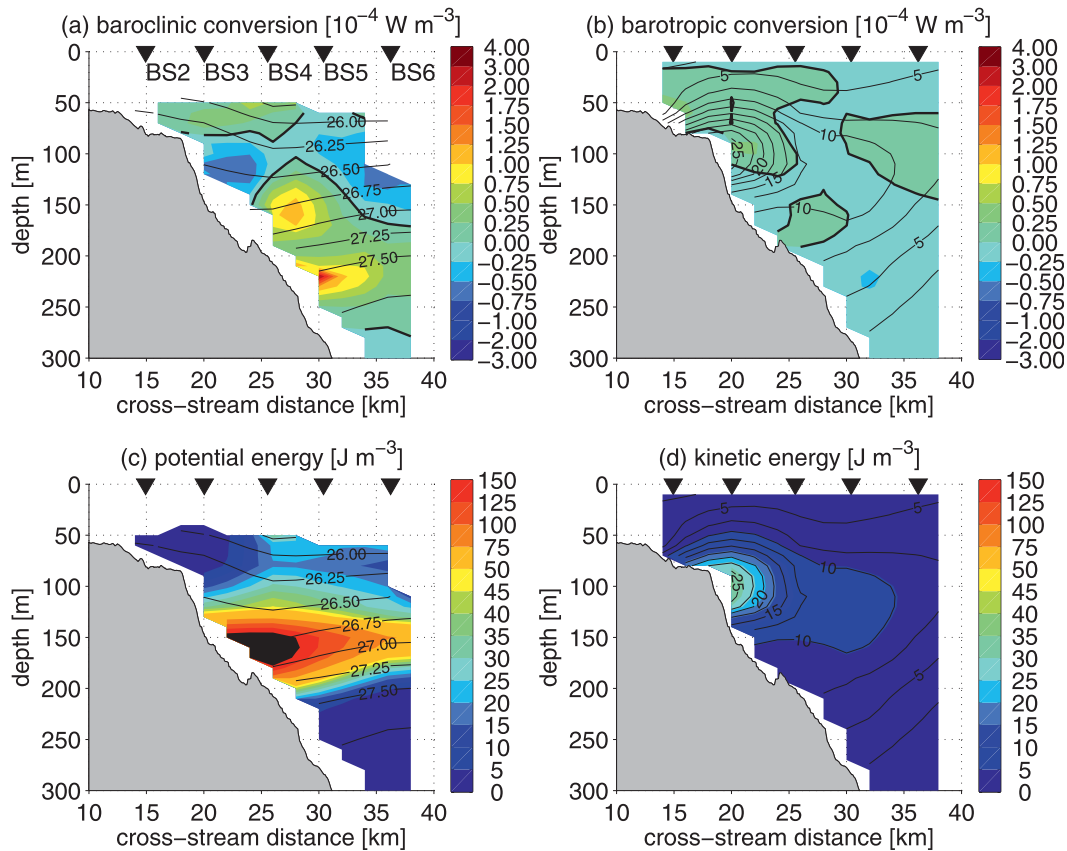


FIG. 13. Energetics of the Western Arctic Shelfbreak Current advecting PWW in 2003. Quantities plotted are as in Fig. 11. (a),(b) are adapted from Spall et al. (2008).

unstable, and hence the cross-stream property fluxes are diminished. Correspondingly, the mean available potential energy for the PWW case is larger (by more than a factor of 2) than for the two summer configurations of the current.

Using a numerical model of the winter water configuration of the Western Arctic Shelfbreak Current (whose energetics were similar to those measured for the 2003 PWW case), Spall et al. (2008) concluded that the

shelfbreak current was the source of the cold-core, anticyclonic eddies observed in the southern Canada Basin. Although it is beyond the scope of the present study to implement a numerical model, we can nonetheless make inferences with some degree of confidence based on the calculated energetics of the two summertime configurations of the jet. It is likely that the mixed instability of the ACW shelfbreak jet will lead to the formation of warm-core, surface-intensified eddies of the

TABLE 2. Length of time period  $T_d$  and mean velocity  $\bar{U}$  in the shelfbreak current, baroclinic mean-to-eddy energy conversion  $C$ , barotropic mean-to-eddy energy conversion  $T$ , total mean potential energy  $P$ , total mean kinetic energy  $K$ , exponential time scale of energy loss  $T_e$ , and exponential distance scale of energy loss  $L_e$  are given for the four PSW time periods and the Spall et al. (2008) PWW time period. Values are given with their standard errors taking into account the cross correlation between the time series at the individual grid points, but not accounting for systematic errors. Some of the conversions are not statistically significant. In those cases, the derived time and distance scales have not been calculated but are rather left blank.

	$T_d$ (days)	$\bar{U}$ ( $\text{m s}^{-1}$ )	$C$ ( $\text{W m}^{-3}$ )	$T$ ( $\text{W m}^{-3}$ )	$P$ ( $10^6 \text{ J m}^{-3}$ )	$K$ ( $10^6 \text{ J m}^{-3}$ )	$T_e$ (days)	$L_e$ (km)
ACW2002	35	$0.29 \pm 0.05$	$180 \pm 78$	$102 \pm 34$	$184 \pm 31$	$120 \pm 20$	$12 \pm 4$	$313 \pm 115$
ACW2003	29	$0.28 \pm 0.04$	$148 \pm 270$	$43 \pm 21$	$775 \pm 126$	$188 \pm 28$	—	—
CSW2003	29	$0.20 \pm 0.04$	$192 \pm 65$	$2 \pm 12$	$162 \pm 31$	$102 \pm 14$	$10 \pm 4$	$169 \pm 74$
CSW2004	15	$0.25 \pm 0.05$	$108 \pm 106$	$-56 \pm 36$	$155 \pm 35$	$93 \pm 20$	—	—
PWW2003	57	$0.17 \pm 0.02$	$55 \pm 51$	$-11 \pm 8$	$449 \pm 98$	$65 \pm 7$	$94 \pm 90$	$1388 \pm 1332$

type reported by Pickart and Stossmeister (2008) (such eddies are present in unpublished data as well). Similarly, baroclinic instability of the CSW shelfbreak current should produce warm-core, middepth anticyclones, also observed by Pickart and Stossmeister (2008). Although the ACW and CSW configurations of the current are present for only about one month each, one might expect that their strong baroclinic conversion rates should result in a substantial offshore flux of Alaskan Coastal Water and Chukchi Summer Water. This is consistent with the common occurrence of these water masses throughout the western Arctic (e.g., Steele et al. 2004).

### b. Decay distances and downstream fate

The above information on the energetics of the shelfbreak current at the location of the mooring array makes it possible to infer some aspects of how the current should evolve as it continues to flow eastward along the continental slope. It is of high interest to determine whether the current stays intact and flows into the Canadian Arctic Archipelago—or onward to Fram Strait—versus rapidly spinning down and thereby fluxing its properties into the interior Arctic. Mountain (1974) addressed this issue using synoptic hydrographic measurements of the Western Arctic Shelfbreak Current to the east of Point Barrow and concluded that the jet should lose its momentum over a distance of  $O(100 \text{ km})$ . Here, we use the mooring time series data to investigate the energy budget of the three configurations of the shelfbreak current (ACW, CSW, and PWW).

Before using the data to estimate the time scale over which the current loses its signal, we present a framework for the baroclinic decay using a simple scaling argument. In particular, we use the scale for the cross-stream eddy density flux as derived by Spall (2004),

$$\overline{\rho'v'} \approx \alpha \bar{u} \Delta \rho. \quad (7)$$

Here,  $\alpha$  is a constant nondimensional scaling factor,  $\bar{u}$  is the mean baroclinic alongstream velocity of the shelfbreak current, and  $\Delta \rho$  is the density difference between the current and interior. This difference, divided by a typical width of the current ( $L^y \approx 20 \text{ km}$ ), scales as the horizontal density gradient,

$$\frac{\Delta \rho}{L^y} = \bar{\rho}_y. \quad (8)$$

The time rate of change of the potential energy is the baroclinic conversion as defined in (5). Hence,

$$\frac{dP}{dt} = -C = -g \overline{\rho'v'} \frac{\bar{\rho}_y}{\bar{\rho}_z}. \quad (9)$$

Noting that  $\rho$  as used in (3) is the same as  $\Delta \rho$  in (8), we can use (3) and (7) to substitute  $\overline{\rho'v'}$  and  $\bar{\rho}_z$  in (9),

$$\frac{dP}{dt} = -C \approx -\alpha \frac{\bar{u}}{L^y} P = -\frac{1}{T_e} P. \quad (10)$$

Here we have identified  $T_e = L^y/(\alpha \bar{u})$  as an exponential decay time in the solution to (10). The interpretation is that, following the flow, after a time  $T_e$  only  $1/e$  of the mean available potential energy is left in the shelfbreak current. This is due to the coupling between available potential energy and baroclinic conversion: as the potential energy decreases, there is less energy that the conversion can draw from and therefore it becomes smaller as well.

The above argument assumes that the velocity in the shelfbreak current  $\bar{u}$  remains constant. However, as the total energy in the current decreases, the velocity will also decrease, representing a second-order effect that lengthens the decay time. However, the decay distance will not be affected by this because, as the flow weakens, so does the conversion rate, and these two effects offset each other. This is seen by computing the decay distance, making use of the solution to (10),

$$L_e = \bar{u} \cdot T_e = \frac{L^y}{\alpha}. \quad (11)$$

Although this provides a framework for the baroclinic decay of the current, we are unable to evaluate (11) to compute  $L_e$  because  $\alpha$  is an unknown constant. We can, however, estimate the baroclinic decay distances directly from the mooring data, simply by computing the quotient  $P/C$  [which by (10) is roughly equal to  $T_e$ ] and multiplying this by the mean flow  $\bar{u}$ . Note, however, as seen by the above scaling, that this length scale does not represent a complete draining of the available potential energy from the current but rather an  $e$ -folding decrease.

A scaling similar to (7) does not exist for the cross-stream eddy momentum flux, so we cannot derive a similar framework for the barotropic decay. However, there is also a coupling between the kinetic energy and the barotropic conversion suggesting that the qualitative behavior should be exponential to first order. Therefore, we consider the baroclinic and barotropic decays together in our estimates below. The reader should keep in mind, however, that this estimate only takes into account energy loss due to mesoscale instabilities; there are clearly other processes impacting the fate of the shelfbreak current. In the next subsection, we discuss some of these other factors and assess their importance.

We now proceed to estimate the approximate exponential decay times—defined as  $(P + K)/(C + T)$ —and associated decay distances from the mooring array data.

For the cases when the conversion rates are statistically significant, we have computed the decay times and, using typical advective velocities of the current (defined as an average over the fastest 40 grid points, which comprise roughly 15% of the domain), converted these into distances. The results are shown in Table 2. For the ACW state in 2002, for which the shelfbreak current was both baroclinically and barotropically unstable, the sum of the energies divided by the sum of the conversions leads to a decay time of  $12 \pm 4$  days, which is about a third of the duration for which that current state was observed. Based on the mean velocity in the core of the shelfbreak current ( $\approx 0.3 \text{ m s}^{-1}$ ), this corresponds to a distance of about 300 km beyond the array site. For the CSW state in 2003 (the other case for which the energy conversion rate estimates were statistically significant), the computed decay time is  $10 \pm 4$  days. With a slower mean velocity of  $\approx 0.2 \text{ m s}^{-1}$ , this implies an even shorter decay distance of order 150 km. In contrast to these relatively short  $O(100 \text{ km})$  decay distances for the two summer water configurations of the shelfbreak current, the PWW state in 2003 decays over a substantially longer distance of roughly 1400 km (decay time of 3 months), although the error estimate is larger as well.

To put these estimates into context, we show maps (Figs. 1, 14) that mark each of the three decay distances. As seen, the winter water configuration of the current reaches the region of the Canadian Arctic Archipelago but is still a long distance from the northern tip of Greenland and Nares Strait. By contrast, the estimated decay distance for the ACW state in 2002 (300 km) is less than the distance to the Alaska–Canada border. As such, based on the energetics of the two summertime configurations of the shelfbreak current, it is unlikely that warm Pacific Water should enter the Canadian Arctic Archipelago as a well-defined shelfbreak current.

### c. Limitations of distance estimates

There are several limitations to the above distance estimates. Intrinsic to this calculation is the assumption that the instabilities have reached their maximum amplitude by  $152^\circ\text{W}$  and continue to extract energy from the current in the same qualitative way as measured at the array. If instead the instabilities continue to grow downstream of the array, the energy extraction would be faster, meaning that our decay distances are overestimates. It is also possible that the flow could stabilize farther downstream (i.e., cease to lose energy), in which case our decay distances would be underestimates. We have also assumed that there is no reentrainment of Pacific Water from offshore during the eddy formation process that might reestablish the density gradient and its associated potential energy. Additionally, it has been assumed that there is

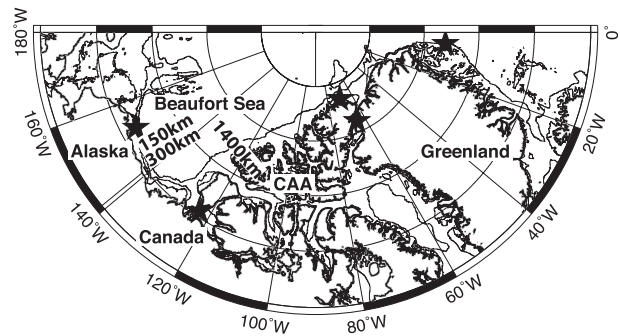


FIG. 14. Map of the Arctic Ocean with the 0-, 50-, 200-, and 1000-m isobaths drawn. The black stars indicate locations mentioned in the text: the mooring array at  $152^\circ\text{W}$  north of Alaska; Amundsen Strait ( $\approx 850 \text{ km}$ ); the Switchyards region north of Ellesmere Island ( $\approx 2600 \text{ km}$ ); Nares Strait between Ellesmere Island and Greenland; and Fram Strait east of Greenland ( $\approx 3600 \text{ km}$ ). Distances are measured from the mooring array following the shelfbreak. Elevation data are from Jakobsson et al. (2008).

no other source of buoyant water to the current; beyond  $135^\circ\text{W}$ , the freshwater from the Mackenzie River might need to be taken into account. We note further that the bathymetry has been assumed uniform in the alongstream direction. Although this is reasonable along the North Slope of Alaska, in the Canadian Beaufort the continental slope becomes significantly steeper. Also, it is not obvious how the shelfbreak current will negotiate the entrance to Amundsen Strait (the first passage into the Canadian Arctic Archipelago).

There is a large-scale pressure gradient between the Pacific and Atlantic (e.g., Woodgate and Aagaard 2005) that drives the throughflow through the Arctic Ocean. However, this pressure gradient does not influence the precise lateral flow patterns by which the Pacific-origin water progresses from Bering Strait to the Canadian Arctic Archipelago and Fram Strait (e.g., via the shelfbreak current or the transpolar drift). This is why we neglect pressure work as an energy source to the evolution of the Pacific Water transport in the shelfbreak current.

We have also neglected friction in the above analysis, which will spin down the current as well. Bottom friction might be especially important for the case of the bottom-intensified CSW and PWW cases. However, buoyancy shutdown in the bottom boundary layer tends to counteract the effect of friction by reducing the bottom stress to zero, which can allow boundary currents to persist for long distances (e.g., MacCready 1994). Brink and Lentz (2010) developed a scaling for the time in which buoyancy shutdown is achieved. Using appropriate values for the Beaufort slope, we find that this should occur rapidly (order of a day). This implies that bottom friction should be negligible for the longer time evolution of the Western Arctic Shelfbreak Current. Frictional spin down by the

ice is another factor that may be at work, particularly for the surface-intensified ACW state. However, in recent decades the ice concentration along the Alaskan Beaufort slope has become near zero over much of the late summer/early fall.

Finally, perhaps the most important limitation to the above analysis is the neglect of wind (recall that periods of wind forcing were excluded from the time series used in the study). In particular, winds may on their own either increase or decrease the potential energy (by changing isopycnal slopes) and kinetic energy (by changing flow velocities). Part of our motivation to focus on the current structure in the absence of wind is that the combined case of external wind forcing and internal mesoscale dynamics is difficult to address. As such, our goal was to isolate the latter with the hope of achieving an incremental but significant improvement in the understanding of this aspect of the shelfbreak current system.

## 6. Discussion

The present study has used high-resolution mooring array data at 152°W from the summers of 2002–04 to investigate the structure, transport, and dynamics of the Western Arctic Shelfbreak Current when it advects Pacific Summer Water in the absence of winds. The jet has two distinct configurations that advect the two major summer water masses, respectively. The Alaskan Coastal Water (ACW) configuration is a surface-intensified shelfbreak current advecting strongly stratified warm and freshwater; it is the extension of the Alaskan Coastal Current that flows through Bering Strait and along the west coast of Alaska in the Chukchi Sea. This configuration of the jet is both baroclinically and barotropically unstable and is estimated to exponentially decay because of the formation of surface-intensified warm-core eddies over a distance of roughly 300 km. The Chukchi Summer Water (CSW) configuration is a bottom-intensified shelfbreak current transporting weakly stratified, less warm, and freshwater that originates in the Bering and Chukchi Seas. It is baroclinically unstable and is estimated to exponentially decay because of formation of mid-depth-intensified warm-core eddies over a distance of roughly 150 km.

The calculated volume transports at 152°W show that, in the mean, between 10% and 20% of the Pacific Summer Water entering Bering Strait reaches the Beaufort Sea as a shelfbreak current. However, in the absence of wind, both configurations of the jet transport on the order of 0.5 Sv to the east. For completeness, we also considered the Pacific Winter Water configuration of the jet studied earlier by Spall et al. (2008). This is a weakly stratified, bottom-intensified current advecting newly formed winter

water near the freezing point. It is also baroclinically unstable but is estimated to decay more slowly over an exponential distance of roughly 1400 km.

Our study has demonstrated that the Western Arctic Shelfbreak Current is an important conduit of Pacific Summer Water downstream of the Chukchi Sea outflow points. Furthermore, its mesoscale dynamics largely dictate the cross-stream flux of freshwater and heat into the interior, which consequently impact the maintenance of the halocline, sea ice melt, and the freshwater reservoir of the Beaufort Gyre. According to our energetics analysis, the mean-to-eddy transfer of energy is so strong that neither of the summer configurations of the current should persist far into the Canadian Beaufort Sea before spinning down. By contrast, the winter configuration seems able to flow into the region of the Canadian Arctic Archipelago (Fig. 1). There are, however, some additional aspects to consider in this regard.

Tracer measurements have detected the presence of Pacific Winter Water in both Nares Strait and Fram Strait (e.g., Jones et al. 2003). This means that either a boundary current provides water to both of these exit points or there is transport of the Pacific Winter Water in the interior basin (e.g., the transpolar drift). If the transport occurs via a boundary current, this would suggest that the above exponential decay distance estimate for the PWW case may be an underestimate. To date, there have been two observational studies near the shelfbreak north of the Canadian Arctic Archipelago. Using a combination of CTD sections and current meter records, Newton and Sotirin (1997) revealed a bottom-intensified eastward flow along the shelfbreak (roughly 200 m deep) in the Lincoln Sea north of Ellesmere Island at the northeastern tip of the archipelago. However, a more recent field program to the west of Nares Strait (the “Switchyards” study; M. Steele 2010, personal communication) found little evidence of a shelfbreak current. It should be noted that in both these studies the cross-stream resolution of measurements is arguably too coarse to properly resolve a shelfbreak current. As such, at this point the observational evidence is inconclusive as to the existence of a Pacific Water boundary current in this region.

There are additional reasons, however, to suspect that the PWW shelfbreak jet does not reach either Nares Strait or Fram Strait. In order for a shelfbreak current to follow a direct path along the shelfbreak from Point Barrow to the Switchyards region, it would have to flow past several entrances to the archipelago that are deeper than 200 m. This raises the question of whether the current would flow into these channels and perhaps back out again or whether it would “jump” such a channel and continue unimpeded along the shelfbreak. Chapman (2003) investigated the conditions under which these two

scenarios occur and found that a relevant factor was the advective distance in a pendulum day (speed of the current divided by the Coriolis frequency) compared to the geometrical dimensions of the channel. By thermal wind, this ratio of the advective distance to the geometrical dimension is related to the width of the current, which was the primary parameter investigated by Sutherland and Cenedese (2009) in a similar study. Amundsen Strait is the first channel into the archipelago that the Western Arctic Shelfbreak Current encounters. The width of the channel is roughly 90 km, and the radius of curvature at its western side is roughly 60 km. Using typical scales of the shelfbreak current at 152°W (noting that these will be overestimates because the current is decaying because of mesoscale instabilities as discussed above), we estimate that both the advective distance and the width of the current are roughly 10 km. This implies that the shelfbreak current would enter Amundsen Strait rather than taking a more direct route across the mouth of the channel.

According to our scaling analysis then, the presence of the different openings to the Canadian Arctic Archipelago drastically increases the effective distance between Barrow Canyon and the Switchyards location along the shelfbreak of the Beaufort and Lincoln Seas. As such, it seems unlikely that the PWW configuration of the jet (and even less so the ACW and CSW configurations) can stay intact all the way to Nares Strait and beyond to Fram Strait. This in turn implies that there are other pathways of Pacific Water feeding these exit points. In this regard, we mention the recent model study of Nguyen et al. (2011), who conclude that the majority of the Pacific Water transport to the northeastern part of the archipelago is accomplished in the transpolar drift. Also, the pan-Arctic model of Aksenov et al. (2011) shows westward flow along the shelfbreak north of the archipelago.

Finally, it is important to keep in mind that our study uses data from a limited time period (2002–04). In light of the pronounced interannual variability in the Arctic system (e.g., associated with the Arctic Oscillation), it is likely that our results are not representative for every summer. For example, the recent study of Watanabe (2011) suggests that, during the latter part of the decade, the summertime shelfbreak jet was weak or nonexistent. Using a numerical model in conjunction with satellite data, Watanabe (2011) compared the shelfbreak jet dynamics in 2003, when the winds over the Chukchi Sea were predominantly northwesterly (because of low pressure over the Beaufort Sea), to 2007 with persistent easterly winds (because of high pressure over the Beaufort Sea). They concluded that the westerly winds enhanced the flux of Pacific Summer Water in the shelfbreak jet during the earlier time period, whereas easterly winds in 2007 transported much of the summer water to

the west in the Chukchi Sea. The latter scenario resulted in cross-shelfbreak Ekman transport of the summer water rather than the formation of a shelfbreak current.

Investigation of the NCEP atmospheric reanalysis fields (Kalnay et al. 1996), as well as measured Quick Scatterometer (QuikSCAT) winds (Naderi et al. 1991) and surface wind measurements at Barrow Airport (Climate-Radar Data Inventories 2010), showed that during the time period of the mooring array (2002–04) typical atmospheric conditions in summer consisted of low pressure over the Beaufort Sea, leading to westerly winds. By contrast, the summers of 2007–09 generally consisted of high pressure over the Beaufort Sea leading to easterly winds in this region. From summer 2008 onward, a mooring at location BS3 (in the center of the shelfbreak jet) has been maintained as part of another field program. Interestingly, the hydrographic time series from July 2008 to August 2009 showed no presence of Alaskan Coastal Water. Based on the above analysis for 2002–04, this mooring should have measured warm ACW within this year-long time frame. Although the absence of ACW in 2008–09 is consistent with the assertion of Watanabe (2011) that the summertime shelfbreak jet is diminished or absent under persistent easterly forcing, this requires more in-depth analysis using the additional mooring data.

*Acknowledgments.* The authors thank K. Brink, M. Spall, M. Steele, and R. Woodgate for helpful discussions and suggestions. T. Weingartner and R. Woodgate provided access to additional SBI mooring data, and M. Steele provided access to the Switchyards hydrographic sections. This work was supported by National Science Foundation Grants OCE-0726640, OPP-0731928, and OPP-0713250.

## REFERENCES

- Aagaard, K., L. Coachman, and E. Carmack, 1981: On the halocline of the Arctic Ocean. *Deep-Sea Res. I*, **28**, 529–545.
- Aksenov, Y., V. V. Ivanov, A. J. G. Nurser, S. Bacon, I. V. Polyakov, A. C. Coward, A. C. Naveira-Garabato, and A. Beszczynska-Moeller, 2011: The Arctic Circumpolar Boundary Current. *J. Geophys. Res.*, **116**, C09017, doi:10.1029/2010JC006637.
- Brink, K. H., and S. J. Lentz, 2010: Buoyancy arrest and bottom Ekman transport. Part I: Steady flow. *J. Phys. Oceanogr.*, **40**, 621–635.
- , F. Bahr, and R. K. Shearman, 2007: Alongshore currents and mesoscale variability near the shelf edge off northwestern Australia. *J. Geophys. Res.*, **112**, C05013, doi:10.1029/2006JC003725.
- Cavaleri, D., and S. Martin, 1994: The contribution of Alaskan, Siberian, and Canadian coastal polynyas to the cold halocline layer of the Arctic Ocean. *J. Geophys. Res.*, **99** (C9), 18 343–18 362.
- Chao, S.-Y., and P.-T. Shaw, 1996: Initialization, asymmetry, and spindown of Arctic eddies. *J. Phys. Oceanogr.*, **26**, 2076–2092.

- , and —, 1998: Eddy maintenance and attrition in a vertically sheared current under Arctic ice. *J. Phys. Oceanogr.*, **28**, 2427–2443.
- , and —, 1999: Close interactions between two pairs of helon-like vortices under sea ice. *J. Geophys. Res.*, **104**, 23 591–23 605.
- Chapman, D., 2003: Separation of an advectively trapped buoyancy current at a bathymetric bend. *J. Phys. Oceanogr.*, **33**, 1108–1121.
- Climate-Radar Data Inventories, 2010: Barrow Post Rogers Airport weather station. NOAA National Climatic Data Center Tech. Rep. [Available online at <http://www4.ncdc.noaa.gov/cgi-win/wwcgi.dll?wwDI~StnSrch~StnID~20022476>.]
- D'Asaro, E., 1988a: Generation of submesoscale vortices: A new mechanism. *J. Geophys. Res.*, **93** (C6), 6685–6693.
- , 1988b: Observations of small eddies in the Beaufort Sea. *J. Geophys. Res.*, **93** (C6), 6669–6684.
- Environmental Working Group, 1998: Joint U.S.-Russian atlas of the Arctic Ocean for the summer period. National Snow and Ice Data Center CD-ROM.
- Grebmeier, J. M., and H. R. Harvey, 2005: The western Arctic Shelf–Basin Interactions (SBI) project: An overview. *Deep-Sea Res. II*, **52** (24–26), 3109–3115, doi:10.1016/j.dsr2.2005.10.004.
- Hall, M., 1994: Synthesizing the Gulf Stream thermal structure from XBT data. *J. Phys. Oceanogr.*, **24**, 2278–2287.
- Huang, R., and R. Schmitt, 1993: The Goldsbrough-Stommel circulation of the world oceans. *J. Phys. Oceanogr.*, **23**, 1277–1284.
- Hunkins, K., 1974: Subsurface eddies in the Arctic Ocean. *Deep-Sea Res. I*, **21**, 1017–1033.
- Jakobsson, M., R. Macnab, L. Mayer, R. Anderson, M. Edwards, J. Hatzky, H. W. Schenke, and P. Johnson, 2008: An improved bathymetric portrayal of the Arctic Ocean: Implications for ocean modeling and geological, geophysical and oceanographic analyses. *Geophys. Res. Lett.*, **35**, L07602, doi:10.1029/2008GL033520.
- Jones, E. P., J. H. Swift, L. G. Anderson, M. Lipizer, G. Civitarese, K. K. Falkner, G. Kattner, and F. McLaughlin, 2003: Tracing Pacific water in the North Atlantic Ocean. *J. Geophys. Res.*, **108**, 3116, doi:10.1029/2001JC001141.
- Kalnay, E., and Coauthors, 1996: The NCEP/NCAR 40-Year Reanalysis Project. *Bull. Amer. Meteor. Soc.*, **77**, 437–471.
- MacCready, P., 1994: Frictional decay of abyssal boundary currents. *J. Mar. Res.*, **52**, 197–217, doi:10.1357/0022240943077073.
- Manley, T. O., and K. Hunkins, 1985: Mesoscale eddies of the Arctic Ocean. *J. Geophys. Res.*, **90** (C3), 4911–4930.
- Mountain, D. G., 1974: Bering Sea Water on the north Alaskan shelf. Ph.D. thesis, University of Washington, 153 pp.
- Muench, R. D., J. D. Schumacher, and S. A. Salo, 1988: Winter currents and hydrographic conditions on the northern central Bering Sea shelf. *J. Geophys. Res.*, **93** (C1), 516–526.
- , J. T. Gunn, T. E. Whittedge, P. Schlosser, and W. Smethie Jr., 2000: An Arctic Ocean cold core eddy. *J. Geophys. Res.*, **105** (C10), 23 997–24 006.
- Naderi, F., M. Freilich, and D. Long, 1991: Spaceborne radar measurement of wind velocity over the ocean—An overview of the NSCAT scatterometer system. *Proc. IEEE*, **79**, 850–866.
- Newton, J., and B. Sotirin, 1997: Boundary undercurrent and water mass changes in the Lincoln Sea. *J. Geophys. Res.*, **102** (C2), 3393–3403.
- Nguyen, A. T., D. Menemenlis, and R. Kwok, 2011: Arctic ice-ocean simulation with optimized model parameters: Approach and assessment. *J. Geophys. Res.*, **116**, C04025, doi:10.1029/2010JC006573.
- Nikolopoulos, A., R. S. Pickart, P. S. Fratantoni, K. Shimada, D. J. Torres, and E. P. Jones, 2009: The western Arctic boundary current at 152°W: Structure, variability, and transport. *Deep-Sea Res. II*, **56**, 1164–1181.
- Ou, H., and A. Gordon, 1986: Spin-down of baroclinic eddies under sea ice. *J. Geophys. Res.*, **91**, 7623–7630.
- Overland, J., and A. Roach, 1987: Northward flow in the Bering and Chukchi Seas. *J. Geophys. Res.*, **92** (C7), 7097–7105.
- Panteleev, G., D. A. Nechaev, A. Proshutinsky, R. Woodgate, and J. Zhang, 2010: Reconstruction and analysis of the Chukchi Sea circulation in 1990–1991. *J. Geophys. Res.*, **115**, C08023, doi:10.1029/2009JC005453.
- Paquette, R., and R. Bourke, 1981: Ocean circulation and fronts as related to ice melt-back in the Chukchi Sea. *J. Geophys. Res.*, **86** (C5), 4215–4230.
- Pickart, R. S., and G. Stossmeister, 2008: Outflow of Pacific water from the Chukchi Sea to the Arctic Ocean. *Chin. J. Polar Oceanogr.*, **19**, 135–148.
- , T. J. Weingartner, L. J. Pratt, S. Zimmermann, and D. J. Torres, 2005: Flow of winter-transformed Pacific water into the western Arctic. *Deep-Sea Res. II*, **52** (24–26), 3175–3198, doi:10.1016/j.dsr2.2005.10.009.
- , G. W. K. Moore, D. J. Torres, P. S. Fratantoni, R. A. Goldsmith, and J. Yang, 2009: Upwelling on the continental slope of the Alaskan Beaufort Sea: Storms, ice, and oceanographic response. *J. Geophys. Res.*, **114**, C00A13, doi:10.1029/2008JC005009.
- , and Coauthors, 2010: Evolution and dynamics of the flow through Herald Canyon in the western Chukchi Sea. *Deep-Sea Res. II*, **57** (1–2), 5–26, doi:10.1016/j.dsr2.2009.08.002.
- , M. A. Spall, G. W. K. Moore, T. J. Weingartner, R. A. Woodgate, K. Aagaard, and K. Shimada, 2011: Upwelling in the Alaskan Beaufort Sea: Atmospheric Forcing and local versus non-local response. *Prog. Oceanogr.*, **88**, 78–100, doi:10.1016/j.pocean.2010.11.005.
- Sambrotto, R., J. Goering, and C. McRoy, 1984: Large yearly production of phytoplankton in the western Bering Strait. *Science*, **225**, 1147–1150.
- Schauer, U., and A. Beszczynska-Möller, 2009: Problems with estimation and interpretation of oceanic heat transport—Conceptual remarks for the case of Fram Strait in the Arctic Ocean. *Ocean Sci.*, **5**, 487–494.
- Shimada, K., E. Carmack, K. Hatakeyama, and T. Takizawa, 2001: Varieties of shallow temperature maximum waters in the Western Canadian Basin of the Arctic Ocean. *Geophys. Res. Lett.*, **28**, 3441–3444.
- Spall, M. A., 2004: Boundary currents and watermass transformation in marginal seas. *J. Phys. Oceanogr.*, **34**, 1197–1213.
- , and J. Pedlosky, 2008: Lateral coupling in baroclinically unstable flows. *J. Phys. Oceanogr.*, **38**, 1267–1277.
- , R. S. Pickart, P. Fratantoni, and A. Plueddemann, 2008: Western Arctic shelfbreak eddies: Formation and transport. *J. Phys. Oceanogr.*, **38**, 1644–1668.
- Steele, M., J. Morison, W. Ermold, I. Rigor, M. Ortmeyer, and K. Shimada, 2004: Circulation of summer Pacific halocline water in the Arctic Ocean. *J. Geophys. Res.*, **109**, C02027, doi:10.1029/2003JC002009.
- Sutherland, D., and C. Cenedese, 2009: Laboratory experiments on the interaction of a buoyant coastal current with a canyon: Application to the East Greenland Current. *J. Phys. Oceanogr.*, **39**, 1258–1271.
- Swift, J., and L. Codispoti, 2003: NBP03-04a service group bottle data documentation. Scripps Institution of Oceanography Tech. Rep., 59 pp. [Available online at [http://data.eol.ucar.edu/datafile/nph-get/62.118/3206NBP0304A\\_final.pdf](http://data.eol.ucar.edu/datafile/nph-get/62.118/3206NBP0304A_final.pdf).]

- Timmermans, M., J. Toole, A. Proshutinsky, R. Krishfield, and A. Plueddemann, 2008: Eddies in the Canada Basin, Arctic Ocean, observed from ice-tethered profilers. *J. Phys. Oceanogr.*, **38**, 133–145.
- Watanabe, E., 2011: Beaufort shelfbreak eddies and shelf-basin exchange of Pacific summer water in the western Arctic Ocean detected by satellite and modeling analyses. *J. Geophys. Res.*, **116**, C08034, doi:10.1029/2010JC006259.
- , and H. Hasumi, 2009: Pacific Water transport in the western Arctic Ocean simulated by an eddy-resolving coupled sea ice–ocean model. *J. Phys. Oceanogr.*, **39**, 2194–2211.
- Weingartner, T., D. Cavalieri, K. Aagaard, and Y. Sasaki, 1998: Circulation, dense water formation, and outflow on the northeast Chukchi shelf. *J. Geophys. Res.*, **103** (C4), 7647–7661.
- , S. Danielson, and T. Royer, 2005: Freshwater variability and predictability in the Alaska Coastal Current. *Deep-Sea Res. II*, **52** (1–2), 169–191.
- Winsor, P., and D. C. Chapman, 2004: Pathways of Pacific water across the Chukchi Sea: A numerical model study. *J. Geophys. Res.*, **109**, C03002, doi:10.1029/2003JC001962.
- Woodgate, R. A., and K. Aagaard, 2005: Revising the Bering Strait freshwater flux into the Arctic Ocean. *Geophys. Res. Lett.*, **32**, L02602, doi:10.1029/2004GL021747.
- , —, and T. J. Weingartner, 2005a: A year in the physical oceanography of the Chukchi Sea: Moored measurements from autumn 1990–1991. *Deep-Sea Res. II*, **52** (24–26), 3116–3149, doi:10.1016/j.dsr2.2005.10.016.
- , —, and —, 2005b: Monthly temperature, salinity, and transport variability of the Bering Strait through flow. *Geophys. Res. Lett.*, **32**, L04601, doi:10.1029/2004GL021880.
- , T. Weingartner, and R. Lindsay, 2010: The 2007 Bering Strait oceanic heat flux and anomalous Arctic sea-ice retreat. *Geophys. Res. Lett.*, **37**, L01602, doi:10.1029/2009GL041621.